



# POLITECNICO MILANO 1863

## Space Propulsion

**Professor:** Filippo Maggi  
Academic year 2023-2024

## Design of a Bi-Propellant Blowdown Liquid Rocket Engine

Authors: Heets Transfer		
Person Code	Surname	Name
10710744	Bellini	Davide
10726411	Bergamaschi	Camilla
10725818	Biraghi	Giacomo
10711761	Cattaneo	Marco
10737865	De Marco	Mattia
10795356	Frassinella	Luca
10990413	Massini	Alessandro
10706185	Mensi Weingrill	Edoardo
10697668	Scudier	Gianluca

---

## Abstract

This paper presents the description of the process that the authors have followed to complete the design of a bipropellant (LOX-RP1) Liquid Rocket Engine with blowdown pressurization system.

The team has organized its work starting from the nominal sizing, based on the initial conditions. This has given the geometrical design of the system which serves as foundations for the whole process. Subsequently, the team implemented the engine evolution in time to evaluate its performance, studying thoroughly the blowdown system. Key considerations have been done particularly regarding pressure losses in the engine: feeding lines, injection and cooling system represent important pressure drops that have to be studied deeply.

The concluding sections of the paper feature two in-depth analyses concerning the cooling system and additive manufacturing. In particular, the first study delves into the cooling system's capability to maintain engine temperature using the fuel throughout the operating time. The second elaboration, on the other hand, is related to the fact that the engine is printed with additive manufacturing without any further refinement: this constraint imposes uncertainties that must be studied, in particular in small orifices like in the injection plate.

## Contents

<b>List of Tables</b>	<b>VII</b>
<b>List of Figures</b>	<b>VIII</b>
<b>1 Introduction</b>	<b>1</b>
<b>2 Literature Review</b>	<b>2</b>
2.1 Blowdown System . . . . .	2
2.2 Additive Manufacturing . . . . .	3
2.3 Nozzle Losses . . . . .	5
<b>3 Technical Approach</b>	<b>7</b>
3.1 Nominal Thermodynamic Parameters . . . . .	7
3.2 Nominal Engine . . . . .	8
3.3 Injectors Design . . . . .	9
3.4 Pressure Losses . . . . .	9
3.5 Tanks . . . . .	10
3.6 Blowdown Ratio . . . . .	10
3.7 Blowdown Iterative Process . . . . .	11
3.8 Uncertainties and Tolerances in Additive Manufacturing . . . . .	12
3.9 Cooling . . . . .	13
3.9.1 Modelling of Cooling Process . . . . .	13
<b>4 Results</b>	<b>14</b>
4.1 Nominal Engine Sizing . . . . .	14
4.2 Nozzle Efficiency . . . . .	15
4.3 Tanks Sizing . . . . .	16
4.3.1 Elliptic Headed Tanks . . . . .	17
4.4 Nominal Configuration Results . . . . .	18
4.5 Mass Budget . . . . .	19
4.6 Injectors Results . . . . .	20
4.7 Analysis of Geometric Tolerances and $C_d$ Variations . . . . .	20
4.8 Cooling Results . . . . .	21
4.9 Sizing of the Regenerative Cooling System . . . . .	22
Layers Thickness . . . . .	22
Tubes Design . . . . .	22
4.9.1 Initial Cooling Validation . . . . .	23
4.9.2 Cooling Compliancy during operative life . . . . .	23
4.9.3 Radiative Cooling . . . . .	23
<b>5 Final Considerations</b>	<b>24</b>
<b>6 Conclusion</b>	<b>25</b>
<b>A Blowdown cycle flux diagram</b>	<b>i</b>
<b>B Cooling</b>	<b>ii</b>
<b>C Nominal design architecture</b>	<b>iv</b>
<b>D Elliptic Headed Tanks Alternative</b>	<b>v</b>

<b>E Engine CFD simulation</b>	vii
<b>F References</b>	ix
<b>G Authorship Declaration</b>	xiii

## Nomenclature

$\alpha$	Convergent angle
$\beta$	Divergent angle
$\dot{m}$	Mass flow rate
$\dot{m}_{fuel}$	Fuel mass flow rate
$\dot{m}_{ox}$	Oxidizer mass flow rate
$\epsilon$	Rhenium emissivity
$\frac{O}{F}$	Oxidizer to Fuel ratio
$\gamma$	Specific heat ratio
$\lambda$	Conductive heat transfer coefficient
$\bar{R}$	Specific gas constant
$\rho$	Density
$\rho_{fuel}$	Fuel density
$\rho_{ox}$	Oxidizer density
$\sigma$	Boltzmann constant
$\sigma^y$	Yield strength
$\theta_{in}$	Inlet angle
$\theta_{out}$	Outlet angle
$\varepsilon$	Expansion ratio
$\varepsilon_c$	Contraction ratio
$A_c$	Combustion chamber area
$A_e$	Exit area
$A_t$	Throat area
$A_{inj}$	Injector area
$A_{pipe}$	Pipe area
$A_{side}$	Side area
$A_{tube}$	Cooling Tubes area
$c^*$	Characteristic velocity
$c_T$	Thrust coefficient
$C_d$	Discharge Coefficient
$D_c$	Combustion chamber diameter

$D_e$	Exit diameter
$D_t$	Throat diameter
$D_{hydr}$	Hydraulic diameter
$D_{pipe}$	Pipe diameter
$D_{tube}$	Cooling jacket tube diameter
$e_w$	Welding efficiency
$f$	Friction factor
$h_g$	Gas side convective heat transfer coefficient
$h_{available}$	Total available height
$h_{co}$	Coolant side convective heat transfer coefficient
$h_{empty-space}$	Height of empty space for pipelines
$H_{global}$	Global thermal resistance
$h_{int}$	Tank internal height
$He$	Helium
$I_{sp_{vac}}$	Gravimetric specific impulse in vacuum
$I_{sp}$	Gravimetric specific impulse
$I_{tot}$	Total Impulse
$k$	Valves' pressure loss factor
$K_{cool}$	Cooling loss coefficient
$K_{head}$	Head loss coefficient
$K_{inj}$	Injection loss coefficient
$K_{tank}$	Tank loss coefficient
$K_{valve}$	Valve loss coefficient
$L^*$	Characteristic length
$L_c$	Combustion chamber length
$L_{conv}$	Nozzle convergent length
$L_{div}$	Nozzle divergent length
$L_{pipe}$	Pipe length
$M$	Mass
$M_c$	Mach number in combustion chamber
$m_{mol}$	Molar mass
$N_{tubes}$	Number of cooling jacket tubes

$Nu$	Nusselt number
$P_c$	Combustion chamber pressure
$P_t$	Throat pressure
$P_{tank}$	Tank pressure
$Pr$	Prandtl number
$q$	Heat flux per unit surface
$q_{rad}$	Radiative Heat flux per unit surface
$r_{curv}$	Curvature radius of the contour nozzle at the throat
$r_{int}$	Tank internal radius
$Re$	Reynolds number
$Re'$	Modified Reynolds number
$T$	Thrust
$t_0$	Initial Time Instant
$T_c$	Combustion chamber temperature
$T_{aw}$	Adiabatic wall Temperature
$T_{bond}$	Bond coating Temperature
$T_{end_{chamber}}$	Fuel Temperature at the end of the combustion chamber (cooling jacket)
$T_{end_{cooling}}$	Fuel Temperature at the end of the cooling jacket
$T_{fuel}$	Fuel Temperature
$T_{inlet}$	Cooling Jacket Inlet Fuel Temperature
$t_{res}$	Residence Time
$T_{tank}$	Tank temperature
$T_{TBC}$	Thermal Barrier Coating Temperature
$T_{w_{co}}$	Engine Wall Temperature (coolant side)
$T_w$	Engine Wall Temperature
$th$	Tank wall thickness
$V$	Volume
$V_c$	Combustion chamber volume
$v_e$	Exit velocity
$V_{available}$	Total available volume
$V_{gas}$	Gas Volume
$V_{ratio}$	Tank volume ratio

AM	Additive Manufacturing
LOX	Liquid oxygen
LRE	Liquid Rocket Engine
NASA	National Aeronautics and Space Administration
PBF	Powder-Bed Fusion
RP1	Rocket propellant 1
SLM	Selective Laser Melting

**List of Tables**

1	Nominal Thermodynamic Parameters for $O/F = 2.2778$ . . . . .	7
2	Nominal NASA CEA results . . . . .	14
3	Areas and diameters . . . . .	14
4	Rao angles and radius of curvature . . . . .	14
5	Engine lengths . . . . .	14
6	Mass flow rates . . . . .	15
7	Initial values of correction factors and thrust . . . . .	16
8	$Ti - 6Al - 4V$ parameters . . . . .	16
9	Helium parameters . . . . .	17
10	Sizing of cylindrical tanks . . . . .	17
11	Comparison of the masses with different materials . . . . .	17
12	Sizing of headed tanks . . . . .	17
13	Thickness in different surfaces of headed tanks . . . . .	18
14	Masses of the propulsion system . . . . .	20
15	Injectors parameters . . . . .	20
16	Materials Thermal Conductivity . . . . .	22
17	Material limit temperatures . . . . .	22
18	Layers thickness . . . . .	22
19	Tubes size . . . . .	23
20	Temperatures of RP1 during Nominal Cooling . . . . .	23
21	RP1 Thermodynamical Properties . . . . .	ii
22	Sizing of elliptic headed oxidizer tank . . . . .	v

## List of Figures

1	<i>O/F ratio</i> vs $c^*$	7
2	Engine 3D CAD representation	8
3	Maximum burning time as a function of the blowdown ratio	11
4	Equivalent electric circuit of the heat transfer model	14
5	Total temperature CFD Simulation	15
6	Blowdown: Thrust evolution	18
7	Blowdown: Chamber pressure evolution	18
8	Blowdown: Mass flow rates evolution	18
9	Blowdown: <i>O/F</i> evolution	18
10	Blowdown: Vacuum specific impulse evolution	19
11	AM Tolerances: Thrust evolution	21
12	AM Tolerances: Chamber pressure evolution	21
13	AM Tolerances: Mass flow rates evolution	21
14	AM Tolerances: <i>O/F</i> evolution	21
15	$T_{end_{cooling}}$ time evolution	24
16	$\dot{m}_{fuel}$ time evolution	ii
17	Sizing of the tubes hydraulic diameter	ii
18	Cooling at $t_0$ flowchart	iii
19	Nominal architecture: External view	iv
20	Nominal architecture: Internal view	iv
21	Knuckles stress factor (Table from page 338 Ref. [1])	v
22	Elliptic headed tank: External view	v
23	Elliptic headed tank: Internal view	vi
24	Total pressure CFD Simulation	vii
25	Total energy CFD Simulation	viii

## 1 Introduction

*"Engineering is the art of transforming difficult problems into simple solutions" - Elon Musk, probably*

The primary objective of this report is to outline the design process of a Liquid Rocket Engine (LRE) and conduct a comprehensive analysis of its performance characteristics. The aim is to establish, through an exhaustive review of the existing literature, a solid foundation of knowledge and best practices in LRE design, which will inform the engineering decisions and methodologies. Following the literature review, it will be presented the step-by-step process adopted by the team in the design, development and testing phases of the LRE. Furthermore, the report will provide an analysis of the performance metrics of the LRE. Throughout the report, insightful comments and justifications will be provided to elucidate the rationale behind our design decisions.

The design of the engine is based on the following constraints on the LRE given by the company:

- The LRE is a liquid semi-cryogenic engine, based on LOX-RP1 propellant to be operated in vacuum.
- The system is a blowdown.
- The system is based on additive manufacturing production.
- The storage has to be done in two blowdown tanks.
- The available volume is 80% of a cylinder with dimensions: 1m (diameter) x 2m (height).
- Initial thrust :  $T = 1 \text{ kN}$ .
- Initial combustion chamber pressure:  $P_c = 50 \text{ bar}$ .
- Minimum allowable chamber pressure  $P_{c_{min}} = 20 \text{ bar}$ .

The company also required:

- To evaluate for the nominal configuration the time profile of thrust, specific impulse and compute the total impulse including losses.
- To verify if the engine can be cooled with RP1 during its all operative life.
- To quantify the expected effect produced by the uncertainties in the additive manufacturing of the injection plate, if no post-machining refinement is performed.

## 2 Literature Review

### Literature Sources

This paper is meant to describe the process followed by the authors to complete the design of the given propulsion systems. To accomplish this task, the team has based its knowledge on the lectures and the notes of Professor F. Maggi and S. Dossi. Starting from this point, it has been searched for further information to enrich and expertise the understanding in the field.

The project is based on different literature collections to explore the available knowledge in the most various and precise way possible. The research systems used to find the biggest amount of useful material were Google Scholar, Research Gate and Aerospace Research Centre: from these websites many articles and books about any of the elements in the propulsion system have been found. Then, the authors mainly based their book library on Biblioteca Politecnico di Milano, La Masa catalogue, where thematic texts are stored. To find precise data regarding single elements such as materials or typical dimensions, producers websites and their data sheets have been consulted.

### 2.1 Blowdown System

The pressurization system aims to control the gas pressure in the propellant's tank. Blowdown is a type of pressurization system in which the pressurizing gas is stored in the propellant tank and its expansion makes the propellant flow up to the combustion chamber; the tank is pressurized to an initial level and pressure decays over time as the propellant is consumed, causing the tank pressure, thrust and propellant flow rate to reduce in time<sup>[2]</sup>. The flow rate from the propellant tank to the combustion chamber is function of the hydraulic losses in the feeding lines<sup>[2]</sup>, which need to be appropriately modelled.

The advantages of the blowdown system lie in its simplicity and reliability due to a small amount of components - this peculiarity also makes it less expensive than other pressurization systems. On the other hand, the main disadvantage of this system is that the tank pressure, thrust and propellant flow rate change as a function of time<sup>[2]</sup>. Other disadvantages, specific for bipropellants, are related to the fact that the blowdown system does not imply a regulation of the pressure, leading to less accurate O/F ratio control, which might cause higher residual propellant with respect to regulated pressure systems<sup>[3]</sup>. A further complexity lies in the combustion and feed system stability under the latter low pressure conditions of the blowdown<sup>[4]</sup>. The variability of propellant flow rate and engine inlet pressure is the reason why the blowdown system is difficult to be used with bipropellant systems and its application is under study, while it is widely used with monopropellant systems since, in that case, the disadvantages are slight<sup>[2]</sup>.

Important considerations can be done to select the pressurizing gas, considering the interaction between the liquid propellant and the pressurizing gas itself, which are in direct contact in a blowdown system<sup>[4]</sup>. The pressurizing gas must be inert and low soluble in presence of the liquid propellants<sup>[3]</sup> and it should have a contained molecular mass; typically, choice falls between Helium or Nitrogen<sup>[2][3]</sup>. Although Helium permits the lightest system, its leakage is difficult to prevent; on the other hand, Nitrogen can be used in the case that weights allow it<sup>[2]</sup>.

Heat exchange between pressurizing gas and liquid propellant leads to condensation of the gas and vaporization of the liquid. In fact, evaporation of the propellant at the gas-liquid interface dilutes the gas, resulting in changes in the gas expansion properties; on the other hand, condensation of gas can dilute the propellant<sup>[3]</sup>. Studies have been conducted to investigate the heat transfer characteristics between the pressurizing gas and the liquid oxidizer in a blowdown system<sup>[5]</sup>, concluding that the presence of the oxidizer vapour pressure should not have a considerable effect on estimated performances and impulse.

Since the blowdown system behaviour depends on the pressure in the tanks, considerations can be done on the thermodynamics of the pressurizing gas. The ratio of initial pressure to final pressure is defined as the blowdown ratio  $B$ , and its maximum value is limited by the inlet pressure range that the engine can accept. The flight cases reported in literature are referred to monopropellant blowdown systems; typical values of  $B$  are between three and four, but lower values (e.g.  $B = 1.8$ ) and higher values (e.g.  $B = 6$ ) have been flown<sup>[2]</sup>. The ideal gas model is used to describe the thermodynamic

properties of the pressurizing gas in steady-state conditions and to predict their evolution in time during the blowdown; normally, the difference between real and ideal gas behaviour is negligible<sup>[2][6]</sup>. Two distinct types of gas transformation – either isothermal or isentropic – are considered to evaluate the pressurizing gas expansion in a blowdown system. Under isothermal assumptions, the temperature of the pressurizing gas approximates the liquid propellant's one and decreases almost linearly in time; isothermal conditions prevail when the withdrawn of the propellant is slow. Isentropic model better describes the gas behaviour in the case that the propellant outflow is rapid, and gas temperature faces a decrease in time with a drop well below the propellant temperature; time after the rapid withdrawal of propellant, the gas-liquid system will reach an equilibrium temperature near the liquid propellant's one<sup>[2]</sup>.

## 2.2 Additive Manufacturing

The following paragraph provides a comprehensive literature overview of the current state of Additive Manufacturing processes, with a primary focus on their utilization in the aerospace sector. This review highlights the key advantages and drawbacks of these processes. The subsequent section will focus onto the inherent uncertainty associated with this technique.

Additive Manufacturing is an innovative technology for fabrication of a wide range of structures characterized by complex internal and external shapes, which typically are not feasible with the traditional manufacturing technique<sup>[7]</sup>. It utilizes a layer-by-layer approach based on a common feedstock, typically powder or wire. This feedstock is melted or fused by a heat source and solidifies to produce the final geometry, starting from 3D model built on CAD<sup>[8]</sup>.

Over the last decade, the research into Additive Manufacturing had an exponential growth, mainly due to the several advantages with respect to the traditional techniques. It offers the capability to design highly complex geometries and enables the integration of multiple components without the need for joints, which are typically a source of failure. This ensures lightweighting without compromising the required component performance in terms of mechanical and thermal properties, and a reduction of manufacturing costs and time. This aspect holds significant importance in the aerospace sector, where materials commonly used are metallic alloys, known for their inherent expense and challenging processing requirements.

The primary drawback of this innovative manufacturing technique lies in the multitude of parameters that can influence the quality and characteristics of the resulting products. These parameters encompass factors such as surface roughness, porosity, and the potential presence of residual stresses or internal cracks within the structure. Furthermore, not all materials are compatible with this technique, and substantial post-processing is often necessary to minimize uncertainties<sup>[8]</sup>.

Nowadays several different methods for additive manufacturing are available, each distinguished by the feedstock and heat source employed in the process. In this paper we will focus on Laser powder-bed fusion (L-PBF), and in particular Selective Laser Melting (SLM). A more comprehensive overview of alternative methods can be found in Ref.<sup>[9]</sup>.

SLM utilizes a layer-by-layer powder-bed approach, where a very fine metal powder is melt and then solidified using a laser. The powder is precisely spread and packed according to the CAD design implemented previously. The process is repeated thousands of times, until the full components is manufactured<sup>[7]</sup>. The crucial aspect lies in the spreading and packaging of the powder, as it will determine the density of the component.

The availability of popular aerospace materials such as Aluminum alloys, Nichel alloys, Titanium alloys, and others (see Table 1, pg. 7 in Ref.<sup>[8]</sup>) makes this technique widely employed in the aerospace sector for the manufacturing of small to medium-sized components. In particular, PBF-based AM processes, as SLM, are very interesting for Titanium and Nichel alloys. These are high performance materials, characterized by high thermal resistance, specific strength and compatibility with cryogenic applications. Based on conventional manufacturing methods, they are characterized by high machining costs and a long lead-time. Consequently, PBF can offer significant economic advantages by producing very complex structures at lower costs with less waste<sup>[8][9]</sup>.

Furthermore, it enables fine resolution and superior print quality with respect to other methods, and the fabrication of components with density quality comparable to traditional manufactured parts. Typically, the maximum feature size ranges from 300 to 400 mm, while the minimum is in the range of 0.2 to 0.4 mm. However, drawbacks include the lengthy duration of the process, which restrict its usage to small-medium components, and its high cost<sup>[8][9]</sup>. In addition, post-heat treatments still need to be applied for the release of residual stresses and to fine-tune material properties<sup>[10]</sup>.

For larger components, the Directed Energy Deposition (DED) method is employed, as explained in the following<sup>[7]</sup>.

Focusing on aerospace field, and in particular its space applications as the design and manufacturing of Liquid Rocket Engines, the primary reason why Additive Manufacturing is so well explored in this field is the lead time reduction for components manufacturing. Speaking about the Injector Head of the Ariane 6 rocket, thanks to powder-bed based technologies the construction time have been reduced from 3 months to 35 hours<sup>[11]</sup>. Also the light-weighting of the resulting components is a driver for the employment of AM, as it is crucial in the aerospace sector to enhance the performances and efficiency of the spacecraft. As reported in Ref.<sup>[12]</sup>, thanks to AM they succeeded to lower the weight of a CubeSat bus of 50%. Both of these advantages originate from the capability to consolidate multiple components into a single piece through Additive Manufacturing. This approach reduces assembly operations and diminishes the necessity for joining techniques. This allows to save time, also because there are less components that need to be certified, to reduce the costs and also the mass<sup>[8]</sup>.

For these various reasons, over the past decade, NASA have extensively explored additive manufacturing techniques. They have designed, developed, and tested a wide set of components of Liquid Rocket Engines (LRE), as combustion chamber, channel-wall cooled nozzles, injectors and augmented spark igniters. In this paper we focused on the manufacturing of injectors through SLM method, for a more exhaustive overview of the application of AM in the design and developing of LREs, see Ref.<sup>[7]</sup>.

Liquid propellant rocket engine injectors atomize and mix the fuel with the oxidizer to achieve efficient and stable combustion, ensuring the necessary thrust without compromising hardware durability<sup>[13]</sup>. Moreover, they are engineered to minimize pressure losses while maintaining a stable combustion process<sup>[14]</sup>. Usually, LRE's injectors consist of a multitude of individually fabricated components, which are then assembled using joining techniques<sup>[7]</sup>. All the processes involved in manufacturing a single injector head are lengthy, challenging to manage, require lot of manual work and they imply additional costs<sup>[15]</sup>. Clearly, AM is especially attractive for reducing the cost of manufacturing injectors, as avoids having to deal with all the piece parts and their processing and assembling<sup>[7]</sup>. To underscore the benefits associated with the adoption of AM, numerous practical examples are available. For instance, AVIO, utilizing Powder Bed Fusion (PBF) technology, indicate that typically one of its injectors comprises 80 individual elements, 1 brazing joint, and 8 welding joints, while the injector realized through AM is composed by two single elements and no joints<sup>[14]</sup>. Another example is the injector head of Ariane 6 rocket. Through PBF technology, they were capable of printing the 122 injection nozzles, the base and front plates, and the distribution dome with the corresponding feed pipes for the hydrogen and oxygen fuels as one integrated component<sup>[11]</sup>. In recent years, NASA Marshall Space Flight Center (MSFC) has developed and tested several injectors (see Table 1, pg 9 in Ref.<sup>[7]</sup>) to assess the feasibility of this technology for fabricating these components. They used principally Nichel super-alloy (Inconel 625 and 718, Monel K-500) and different combinations of fuel-oxidizer, and they performed multiple hot-fire tests. A large amount of the tests reported combustion efficiencies comparable with injectors manufactured through traditional techniques<sup>[7]</sup>.

Despite all the benefits listed so far, the inherent complexity of PBF, and in general all metallic AM, introduces various sources of uncertainty that can impact the quality, reliability, and performance of manufactured components. Understanding and mitigating these uncertainties is crucial. The following paragraph of the literature review aims to explore the sources, effects, and mitigation strategies of uncertainty in metallic additive manufacturing processes.

First of all, it is essential to identify the uncertainty sources in Additive Manufacturing processes. Hu, Z., & Mahadevan, S. in the paper Ref.<sup>[16]</sup> propose an uncertainty quantification framework to pre-

dict the material properties when built using AM. They divide the uncertainty sources into two categories: aleatory and epistemic. Aleatory uncertainty refers to nature variability, and -*include natural variability in the radius of the powder particles, fluctuation of laser scan speed, variation of mechanical properties (elasticity, friction coefficient, and damping coefficients) of powder particles, variation of diffusion coefficient of the material, uncertainty of absorption coefficient, variation in the temperature boundary condition, and measurement errors-*. Epistemic uncertainty arises from measurements errors, limited data availability and approximations made in the models (as modeling powder particles as perfect sphere).

The uncertainty related to Additive Manufacturing leads to three main effects: dimensional inaccuracies<sup>[10][17][18]</sup>, micro-structural defects such as porosity due to void formation & non-uniform grain structure<sup>[9]</sup>, surface finish and roughness<sup>[10][17][18][19]</sup>.

J. Ilcik, D. Koutny and D. Palousek dealt with the inspection of the geometric accuracy and the possible tolerances of the parts produced by additive manufacturing in the paper Ref.<sup>[17]</sup>. They performed several tests on different models, using different settings of laser power and scanning speed. The results obtained in terms of geometrical inaccuracy for cylindrical holes are in the order of  $\pm 0.06$  mm, with the best result of  $\pm 0.02$  mm obtained for minimum laser speed and maximum laser power. Regarding the surface roughness of the final product, which is caused by particles of powder adhering to the surface of parts<sup>[10]</sup>, the paper demonstrates how the different slope angles to the machine platform affect the surface finishing, as stated also by ISO/ASTM.52911-1<sup>[10]</sup>. Good surface quality is achieved for angles from  $10^\circ$  to  $130^\circ$ , while for other inclinations post processing is necessary.

P. Keller and R. Mendricky instead focused their work in Ref.<sup>[18]</sup> in investigating the individual parameters affecting the dimensions of the product and the surface quality. In terms of geometrical inaccuracies, the results of the research are in line with the one obtained in Ref.<sup>[17]</sup>, while analyzing the internal tensions generated due to the large quantity of heat involved in the process, they showed that significant deformations occurred.

A comprehensive analysis of the effects of surface roughness resulting from the Selective Laser Melting (SLM) process has been conducted by T. Lieneke-et-al in Ref.<sup>[19]</sup>. They explored, via statistical analysis of the Discharge Coefficient  $C_d$ , how liquid injector elements produced via SLM exhibit flow behavior differing from those produced using traditional machining methods. The paper provides a prediction interval that can be used to forecast a range of  $C_d$  values for injectors with geometries similar to those examined, manufactured using comparable SLM printing technology.

Regarding the micro-structural defects, they are strictly correlated to the nature of the AM process. Indeed, due to the layer-by-layer printing process, the micro-structure of the material within each layer differs from that at the boundaries between layers. This anisotropic behavior leads to varying mechanical properties of the 3D printed part under vertical tension or compression compared to those in the horizontal direction. In metals and alloys, which undergo 3D printing through heat fusion (such as SLS or SLM), the addition of subsequent layers reheats the boundaries of the previous layers. Consequently, this results in a distinct grain micro-structure and anisotropic behavior due to thermal gradients<sup>[20]</sup>.

Uncertainty in metallic additive manufacturing arises from various sources, and they results in dimensional inaccuracies, micro-structural defects, and surface irregularities, impacting the quality and performance of printed parts. However, through post-processing techniques such as cleaning with compressed air and abrasive blasting for powder removal, the latter one for better surface finish and heat treatment to reduce material anisotropy<sup>[10]</sup> these uncertainties can be effectively mitigated, enhancing the reliability, repeatability, and industrial adoption of metallic AM technologies.

Based on the literature review outlined above, an analysis will be conducted in Section 4.7 to assess the impact of Additive Manufacturing uncertainties on the performance of a Liquid Rocket Engine Injector head.

## 2.3 Nozzle Losses

Nozzles play a critical role in a Rocket Propulsion System since their design is crucial in thrust generation and fuel optimization; due to their relevance, several studies have been conducted in order to reach

the best and the most efficient configuration. The entire group of nozzles developed and their peculiar characteristics have been collected by Khare and Saha<sup>[21]</sup> in their paper.

Modelling a nozzle and its effect on the thrust, due to the complexity of the phenomenon, may result a challenging task. This is the reason why, for a preliminary design, is important the concept of *ideal nozzle*<sup>[3]</sup>, characterized by a quasi-one-dimensional, non-reactive flow.

The assumption of ideal flow doesn't take into account the real 3D behaviour and the losses associated therewith<sup>[3]</sup>. The authors focused their research on the experiments and numerical simulations carried out through the years, in order to apply a reasonable Discharge Coefficient  $C_d$  to the ideal performances of the rocket.

The divergence losses, predicted for a simple axial-symmetric nozzle in 1940 by Malina<sup>[22]</sup>, take precedence as the primary subject of analysis. These losses are due to the non-axial component of the exit velocity which doesn't contribute on the thrust<sup>[23]</sup>. For a simple Conical nozzle  $C_d$  is computed from  $C_d = \frac{1+\cos\alpha}{2}$ , where  $\alpha$  is the divergent angle; in Ref.<sup>[23]</sup> are reported analytical computation for more complex 2D nozzles. Since the contour of the analyzed nozzle is retrieved from the Rao approach, authors were interested in the divergence correction factor for a bell nozzle, resulting in  $C_d = \frac{1+\cos(\frac{\alpha+\theta_{out}}{2})}{2}$ , with  $\theta_{out}$  the diverging angle of the bell nozzle and  $\alpha$  the reference conical angle<sup>[24]</sup>.

Due to the order of magnitude of the dimensions involved in the analyzed case, the boundary layer in the proximity of the throat represent a critical region in which both losses<sup>[25]</sup> and heat transfer<sup>[26]</sup> could be very dangerous. Murch's<sup>[25]</sup> paper analyzes losses in both analytical, following Cohen and Reshotko boundary layer theory<sup>[27]</sup>, and experimental. The analysis shows the effect of Reynolds number, and therefore of the viscous component of the flow, on the nozzle efficiency, varying expansion ratio and half-cone angle. Schoenman<sup>[26]</sup> otherwise focuses his attention, starting from existing literature (See Refs<sup>[28][29][30]</sup>), on the prediction of heat transfer in Low-Thrust Nozzle. His paper states, supported by experiments and literature, that laminar boundary layers theory is capable to predict the gas-side heat transfer coefficient in small nozzles.

Tang<sup>[31]</sup> in his paper provides experiments supporting the analysis<sup>[32]</sup> of a flow through a choked axial-symmetric nozzle, leading to a simple equation to retrieve the  $C_d$  as a function of Reynolds number. The experiments conducted confirmed the validity of his analysis, under certain hypothesis. Tang's formula will be used in the following sections (Section 4.2) to compute the global Thrust correction factor.

More recently, the study of the whole parameters impacting on the nozzle efficiency shifted to the exploitation of the modern CFD (Computational Fluid Dynamics) methods. Sabirzyanov<sup>[33]</sup> in his paper performed the discharge coefficient dependence on the nozzle geometry and the presence of a condensed phase in combustion products using the two-equation RNG (Re-Normalisation Group) k- $\epsilon$  model and the four-equation transition SST (Menter's Shear Stress Transport) model.

Another significant loss to consider is the finite-rate dissociation-recombination kinetic loss. This occurs because short nozzle lengths and supersonic flow generate brief residence times in the nozzle and nearly frozen flow. Ideally, gas would reach chemical equilibrium at every point in the nozzle flow field. However, the expanding flow can accelerate gas molecules so rapidly that their residence time in the nozzle is insufficient for full equilibrium to be achieved. This state of thermochemical non-equilibrium leads to variations in specific impulse<sup>[34]</sup>.

The latter can be evaluated through the Two-Dimensional Kinetics (TDK) code of Nickerson, et al. as indicated by Pearson, Brian Landrum and Hawk<sup>[34]</sup>.

According to literature other types of loss exist, for example the loss due to throat erosion, which is typical for solid propulsion systems.

Nevertheless, the authors decided to focus their attention on the most significant for the analyzed case.

### 3 Technical Approach

Given the requirements stated in the Introduction (Section 1) and analysed in the Literature Review (Section 2), the team has developed a code capable to size the full engine at the initial instant and to iterate in time, in order to retrieve the figures of merit evolution (Thrust, Specific Impulse, Combustion Chamber Pressure) at each time instant. To achieve the desired results the authors exploited their theoretical knowledge through the following software: Matlab, NASA Chemical Equilibrium with Application (CEA), Rocket Propulsion Analysis (RPA), Ansys Fluent, Solidworks. In the following sections, the technical approach employed is elucidated. The high-level assumptions chosen by the teams are the following:

- Adiabatic propellant tanks
- Pressurizing gas (Helium) modeled as an ideal gas
- Liquid fuel and oxidizer modeled as incompressible fluids
- Frozen condition in the combustion chamber
- Adiabatic nozzle

The subsequent sections provide a succinct analysis of the cognitive process undertaken to design each component of the engine.

#### 3.1 Nominal Thermodynamic Parameters

The initial objective of the team involves analyzing and determining the most suitable Oxidizer-to-Fuel  $O/F$  ratio for the designated combination of  $RP1$  &  $LOX$ . The optimal  $O/F$  ratio has been found using NASA CEA code Assigned Enthalpy & Pressure Problem. Utilizing an input combustion chamber pressure  $P_c = 50 \text{ bar}$ , along with the designated reactants ( $RP1$  &  $LOX$ ) maintained at their respective storage temperatures ( $T_{RP1} = 298.14 \text{ K}$  and  $T_{LOX} = 90.14 \text{ K}$ ), the computational model retrieves the combustion chamber temperature  $T_c$  and the specific heat ratio  $\gamma$ . From these two parameters, the characteristic velocity  $c^*$  can be retrieved. Figure 1 shows the  $O/F$  ratio vs  $c^*$  curve, and the selected nominal  $O/F$  ratio is the one that maximizes  $c^*$ .

$\gamma [-]$	$T_c [K]$	$M_{mol} [kg/kmol]$	$c^* [m/s]$
1.1724	3383.5	22.52	1737.8

Table 1: Nominal Thermodynamic Parameters for  $O/F = 2.2778$

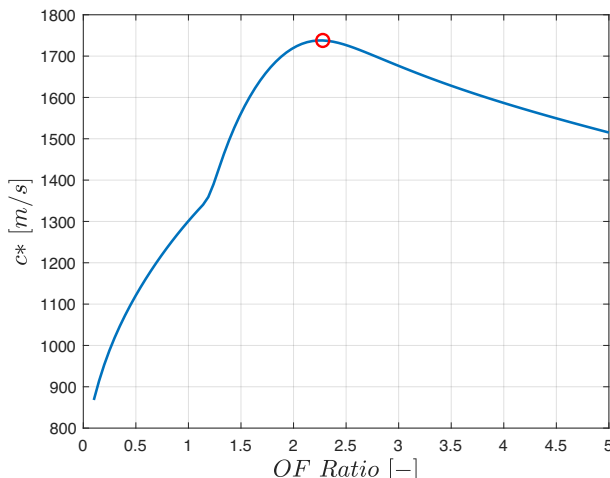


Figure 1:  $O/F$  ratio vs  $c^*$

### 3.2 Nominal Engine

Once selected the optimal  $O/F$  ratio and computed the nominal thermodynamic parameters shown in Table 1, from the nominal condition specified in the requirements it is possible to accurately size the geometry of our engine.

First of all, both the expansion ratio ( $\varepsilon$ ) and contraction ratio ( $\varepsilon_c$ ) must be assumed. Typical literature values in vacuum operating condition for  $\varepsilon$  are  $110 \div 400$ <sup>[35]</sup>, while for  $\varepsilon_c$  are  $5 \div 15$ <sup>[36]</sup>. Using NASA CEA code Rocket Problem, giving as input  $P_c$ , the selected  $O/F$ ,  $\varepsilon$ ,  $\varepsilon_c$  and the designated reactants, the following parameters are retrieved: pressure  $P_e$ , Mach number  $M_e$  and sonic velocity  $a_e$  at the nozzle exit, and the thrust coefficient  $c_T$ .

Then, starting from the computation of the throat area  $A_t$ , knowing the nominal thrust  $T$ , the exit area  $A_e$  and the combustion chamber area  $A_c$  are retrieved via Equation (1):

$$A_t = \frac{T}{P_c c_T} \quad A_e = \varepsilon A_t \quad A_c = \varepsilon_c A_t \quad (1)$$

Then the mass flow rate can be computed via Equation (2):

$$\dot{m} = \frac{P_c A_t}{c^*} \quad (2)$$

From the  $O/F$  ratio is possible to retrieve the mass flow rate of oxidizer  $\dot{m}_{ox}$  and fuel  $\dot{m}_{fuel}$ .

For the design of the combustion chamber, after computing the cross-sectional area, the characteristic length  $L^*$  must be determined. The selection of  $L^*$  involves a trade-off between the need to maximize  $c^*$  by increasing  $L^*$  and ensuring the completeness of the combustion process by decreasing  $L^*$ .

A feasible value of  $L^* = 1,08\text{ m}$  has been selected from Sutton Tables<sup>[3]</sup>, obtaining a residence time of  $t_{res} = 13.1\text{ ms}$ , which falls within the provided feasible range of  $2 \div 40\text{ ms}$ <sup>[36]</sup>. The combustion chamber volume can be retrieved as:  $V_c = L^* A_t$ . Then, knowing the cross-sectional area  $A_c$  of the combustion chamber, the length of the combustion chamber  $L_c$  can be straightforwardly determined.

These outcomes play a fundamental role in implementing the Rao Approach (See Ref.<sup>[37]</sup> for a detailed treatment) for nozzle design. The team has decided to opt for a bell nozzle, despite the presence of other nozzle types that perform better in vacuum, such as the Expansion-Deflection Nozzle<sup>[21]</sup>. This choice is attributed to the bell nozzle's simpler design and the extensive literature available on it. From Rao tables<sup>[36]</sup>,  $\theta_{in} = 38^\circ$  and  $\theta_{out} = 9^\circ$  are selected to characterize the shape of the nozzle and to evaluate the divergence losses.

The results of the nominal geometry are shown in Section 4.3.1.

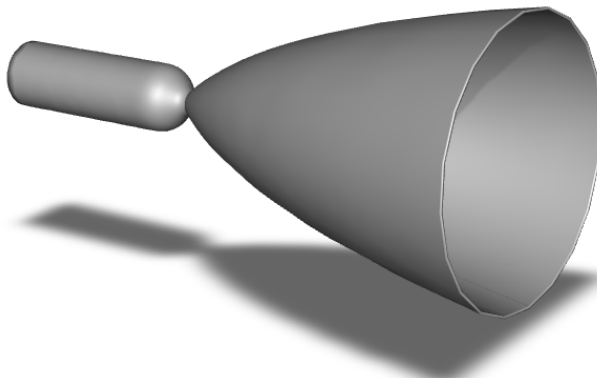


Figure 2: Engine 3D CAD representation

### 3.3 Injectors Design

By analyzing engine parameters, the optimal configuration for the injectors can be determined to achieve efficient mixing and combustion within the combustion chamber.

The selection of the unlike-impinging triplet configuration was based on its ability to achieve effective mixing and atomization through the direct impingement of fuel and oxidizer jets. Indeed, it provides an overall mixing uniformity which is slightly improved with respect to others configuration, for example the unlike-impinging doublet. Furthermore, in order to reduce the heat flux to the wall a reversed design, compared to the classical design, involving two outer fuel jets and a central oxidizer have been used<sup>[13]</sup>.

The configuration, the shape of the injectors and the corresponding discharge coefficient  $C_d$  were chosen according to Refs.<sup>[13][36]</sup> for both fuel and oxidizer, considering that sharp-edged orifices were selected.

The pressure drop across the injection head was fixed as 20% of the combustion chamber pressure and, with it, the total area of the injectors for both the reactants was computed<sup>[36]</sup> via Equation (3):

$$A_{ox,fu}^{tot} = \frac{\dot{m}_{ox,fu}}{C_d \sqrt{2\Delta P \rho_{ox,fu}}} \quad (3)$$

According to evaluations explained in the following Section 4.6 the number of triplets was chosen. Knowing the configuration and its number of orifices, the singular diameter for one reactant has been computed. Checked if it was a feasible value according to additive manufacturing structural constraints, it was possible to evaluate the number of orifices for the other reactant. From this latter value and from the area value, the diameter of the other reactant has been calculated and checked too<sup>[13]</sup>. Another option for the design iteration process would have started from fixing the diameter of one of the reactants and recovering the singular area<sup>[36]</sup>.

The constraint of the additive manufacturing and the operative temperature of the injection head led to the choice of the material, the superalloy Inconel 718.

### 3.4 Pressure Losses

A defined pressure cascade must be granted along the whole feeding line in order to maintain the performance<sup>[36]</sup>. The different contributions, as indicated in Section 3.7, include:

- $\Delta P_{tank} = K_{tank} \dot{m}^2 = \frac{1}{2\rho A_{pipe}^2} \dot{m}^2$ , which indicates a pressure drop due to the flow entering the pipe with a velocity of 10 m/s, starting from a steady state condition in the tank<sup>[36]</sup>.
- $\Delta P_{feed} = \Delta P_{head} + \Delta P_{valve} = K_{head} \dot{m}^2 + K_{valve} \dot{m}^2 = \frac{8}{\pi^2} f \frac{L_{pipe}}{\rho D_{pipe}^5} \dot{m}^2 + \frac{k}{2\rho A_{pipe}^2} \dot{m}^2$ , used to indicate both the losses due to friction along a given length of pipe and to valves and evaluated using the typical approximations for Phase A.
- $\Delta P_{cool} = K_{cool} \dot{m}^2 = \frac{(1-\beta^4) \dot{m}_{fuel}^2}{2\rho_{fuel} (C_{D_{cool}} A_{tube})^2}$ , where  $\beta$  indicates the orifice-to-tubing diameter ratio and  $C_{D_{cool}}$  is the cooling discharge coefficient which has been found knowing  $\beta$  and  $Re$ <sup>[38]</sup>.
- $\Delta P_{inj} = K_{inj} \dot{m}^2 = \frac{8}{\rho} \left( \frac{1}{A_{inj} C_d} \right)^2 \dot{m}^2$ , calculated as  $0.2 P_c$ <sup>[36]</sup>.

In the nominal condition, knowing the initial mass flow rate for both fuel and oxidizer, is possible to retrieve all the constant values presented in the previous equations. In addition, by setting the value of  $v_{pipe} = 10 \text{ m/s}$ , through the continuity shown in Equation (4)

$$\dot{m}_{fuel/ox} = \rho_{fuel/ox} A_{pipe_{fuel/ox}} v_{pipe} \quad (4)$$

it was possible to compute the cross-sectional area of the pipes for both oxidizer and fuel feeding lines.

### 3.5 Tanks

The main constraint about these components is the maximum available volume, which is limited to 80% of the total volume. It is crucial to adhere to this limitation in order to optimize the utilization of available amount of fuel.

Tanks are considered adiabatic and the pressurizing gas is assumed as a perfect gas, hence the expansion of the gas can be modelled via Equation (5). Tanks isolation, coating and liner were not considered.

$$PV^\gamma = \text{const} \quad (5)$$

Initially, the two initial tank pressures  $P_{\text{tank}_{ox/fuel}}$ , were determined by adding the nominal combustion chamber pressure  $P_c$  to all the pressure drops computed in Section 3.4. Obviously, the two  $P_{\text{tank}_{ox/fuel}}$  are different, as along each feeding line the overall pressure drop is different.

Starting from the temperature required to keep the oxidizer and fuel in a liquid state, the search focused on identifying a material capable of withstanding high pressure under both conditions<sup>[39]</sup>. Examining real space applications there were numerous options available for the materials: Steel<sup>[40]</sup>, Aluminum<sup>[40]</sup> and Titanium alloys<sup>[41]</sup>.

The second decision to make is to determine which pressurizing gas is best suited for use, considering the semi-cryogenic conditions. Typically, the options are Helium and Nitrogen, as seen in the Literature (Section 2.1), so in Section 4.3 the analysis was conducted among these two.

Concerning the volumes, the two tanks have distinct capacities. The ratio between them is computed in Equation (6):

$$V_{\text{ratio}} = \frac{\dot{m}_{ox}}{\rho_{ox}} \frac{\rho_{fuel}}{\dot{m}_{fuel}} \quad (6)$$

and so, from the perfect-gas law, it is clear that the initial pressurizing gas volume in each tank is free.

Ultimately, the sizing process has been implemented to target the requirement of the total volume, with additional constraints on the radius of the fuel tank to allow the passage of the pipelines fore the oxidizer. Thanks to a simple equations system which links the volume constraints to the thicknesses ( $th$ ) needed to guarantee structural integrity, the geometrical parameters were obtained for both the tanks ( $th$ ,  $r_{int}$ ,  $h_{int}$ ). Wall thickness was evaluated with Equation (7):

$$th_{ox,fuel} = \frac{r_{int}P}{\sigma^y/1.33} \quad (7)$$

where  $\sigma$  is the value of the yield strength of the material and 1.33 is the safety factor for propellant tanks without hazard to personnel<sup>[1]</sup>.

The literature demonstrates that cylindrical tanks of this type are unsuitable for operation<sup>[1][39]</sup>. In the system calculation, a cylindrical tank with a flat head was employed to accommodate a larger mass of propellant. However, its design is not intended to withstand such high pressures. As shown in many sources<sup>[1][42][43]</sup>, the most compact shape is a cylindrical body with elliptical heads with a ellipse ratio  $a/b = 2$ . The design of this type of tanks has been better explored in the Section 4.3 and in Appendix D. In the computation, the selection of tanks was made based on the case where more propellant could be stored. Although headed tanks result more realistic, the volume occupied is less than the constraint due to their shape, hence it is selected the cylindrical shape.

### 3.6 Blowdown Ratio

The main information of a blowdown pressurization system is the blowdown ratio:

$$B = \frac{P_{\text{gas,in}}}{P_{\text{gas,fin}}} = \frac{P_{\text{tank,in}}}{P_{\text{tank,fin}}} \quad (8)$$

$B$  is defined as the ratio between the initial tank's pressure  $P_{\text{tank,in}}$  and the final tank's pressure  $P_{\text{tank,fin}}$ . The ratio for this engine was found with an optimization study that considered the available

burning time for each different blowdown ratio. The goal of the analysis was to obtain the largest possible burning time for the engine. Hence there were two constraints for the optimization problem: the first one is the minimum allowable pressure in the combustion chamber for the engine working conditions, the second is correlated to the available propellant in the tanks. The team chose to impose the minimum final volume of propellant (both for the fuel and the oxidizer) at least at the 10% of the initial propellant volume<sup>[44]</sup>. From the result, presented in Figure 3, it is chosen a blowdown ratio  $B = 3.1$ , which provides a burning time of  $t_{burn} = 2546\text{ s}$ .

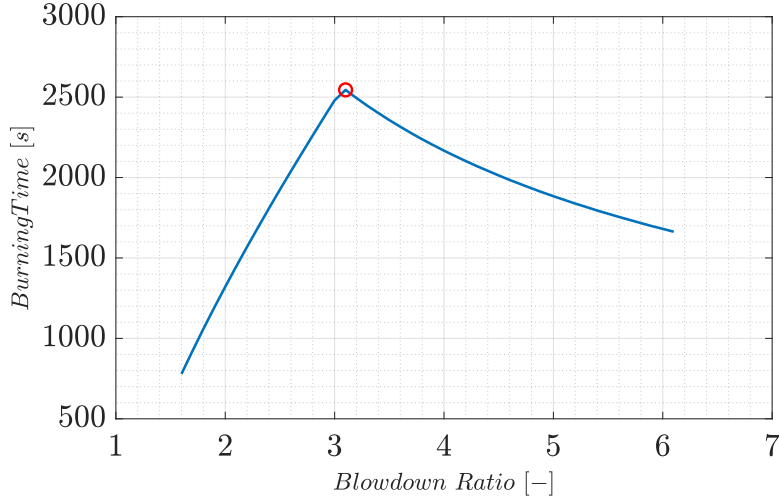


Figure 3: Maximum burning time as a function of the blowdown ratio

### 3.7 Blowdown Iterative Process

The propulsion pressurization system works considering a blowdown concept.

This idea suggests that the tanks contain both the fuel or the oxidizer and the pressurizing gas. Once the engine starts, the pressurizing gas, here Helium (as clarified in Section 4.3), expands following an adiabatic relation and pushes the propellant inside the pipelines, which lead to the combustion chamber. As the expansion proceeds, the gas volume increases, hence the pressure inside the tanks decreases due to the adiabatic behaviour.

Since the maximum pressure is at the starting point, the maximum mass flow rate is also at the beginning, finding that the combustion chamber pressure decreases as the engine runs due to the mass flow rate - chamber pressure relation reported in Equation (9):

$$P_c = \frac{c^* \dot{m}}{A_t} \quad (9)$$

The team modelled the evolution in time of the blowdown system evaluating at each time step the total mass flow rate ( $\dot{m}_{tot}$ ), computing the oxidizer and the fuel mass flow rates, the combustion chamber pressure ( $P_c$ ) and the engine thrust (T).

Given that the evolution in time changes the characteristics in the combustion chamber, at each time step the engine parameters – which are the combustion chamber temperature ( $T_c$ ), the thrust coefficient ( $c_T$ ), the molar mass ( $m_{mol}$ ) and the heat capacity ratio ( $\gamma$ ) – are recomputed using the NASA CEA Matlab function giving as inputs the oxidizer to fuel ratio ( $O/F$ ) and the combustion chamber pressure at the current step. Then, the characteristic velocity at the current time step ( $c_{(i)}^*$ ) is evaluated via Equation (10) (for better readability, the notation used for the current time step ( $i$ ) is suspended inside the square root):

$$c_{(i)}^* = \sqrt{\frac{\frac{R}{m_{mol}} T_c}{k \left(\frac{2}{k+1}\right)^{\frac{k+1}{k-1}}}} \quad (10)$$

Upon receiving the updated combustion chamber profile, the changes in oxidizer and fuel volumes are computed in Equation (11), based on the mass difference between the current ( $i$ ) and the successive ( $i + 1$ ) time steps:

$$V_{(i+1)} = V_{(i)} - \frac{\dot{m}_{(i)}}{\rho} \Delta t \quad (11)$$

From it, having fixed the tanks' total volumes, it is possible to find the pressurizing gas volume.

For the study, the team assumed, as said before, adiabatic expansions, and so, knowing the gas volumes and the heat expansion ratio of the pressurizing gas, it is possible to compute the pressures in the tanks at each time step with the adiabatic relation in Equation (12):

$$P_{\text{tank}_{(i+1)}} = P_{\text{tank}_{(i)}} \left( \frac{V_{\text{gas}_{(i)}}}{V_{\text{gas}_{(i+1)}}} \right)^\gamma \quad (12)$$

The Matlab model now performs the resolution of the system of equations of the combustion chamber pressure, oxidizer and fuel mass flow rates considering the pressure losses:

$$\begin{cases} P_{c_{(i+1)}} = \frac{c_{(i)}^* [\dot{m}_{ox_{(i+1)}} + \dot{m}_{fuel_{(i+1)}}]}{A_t} \\ P_{\text{tank},fuel_{(i+1)}} - P_{c_{(i+1)}} = (K_{\text{tank},fuel} + K_{\text{feed},fuel} + K_{\text{inj},fuel}) \dot{m}_{fuel_{(i+1)}}^2 \\ P_{\text{tank},ox_{(i+1)}} - P_{c_{(i+1)}} = (K_{\text{tank},ox} + K_{\text{feed},ox} + K_{\text{inj},ox}) \dot{m}_{ox_{(i+1)}}^2 \end{cases} \quad (13)$$

The system in Equation (13) is numerically solved with the Matlab function `fsoolve`, which performs the Newton's method for solving systems of equation. After solving the system, the new total mass flow rate and O/F are computed with Equation (14):

$$\dot{m}_{(i+1)} = \dot{m}_{ox_{(i+1)}} + \dot{m}_{fuel_{(i+1)}} \quad \frac{O}{F_{(i+1)}} = \frac{\dot{m}_{ox_{(i+1)}}}{\dot{m}_{fuel_{(i+1)}}} \quad (14)$$

Eventually, it is possible to compute the thrust at every single step (Equation (15)), knowing the current total mass flow rate, the thrust coefficient and the characteristic velocity:

$$T_{(i+1)} = \dot{m}_{(i+1)} C_{T(i)} c_{(i)}^* \quad (15)$$

The cycle is repeated at each step until  $t_{burn}$  is reached. A more clarifying flux diagram is attached in Appendix A.

### 3.8 Uncertainties and Tolerances in Additive Manufacturing

The uncertainties in the additive manufacturing of the injection plate have been evaluated both in terms of geometric tolerances and effects of the increased surface roughness.

The geometric tolerances have been sourced from the datasheet of an existing Metal Additive Manufacturing 3D printer ProX DMP 320<sup>[45]</sup>. This specific 3D printer was selected primarily because it was utilized in the fabrication of the injector head for the European-funded project SMILE LOX/RP1 rocket engine<sup>[46]</sup>, which shares similar specifications with the injector under discussion in this paper.

While to assess the impact of increased surface roughness resulting from additive manufacturing on engine performance, the team referenced a table from the literature<sup>[19]</sup>. In the paper, the authors analyzed the coefficient of discharge  $C_d$  in an injector with a flow circuit design similar to the one adopted by the team. They also outlined the potential uncertainties linked to the obtained values. Due to the absence of the same  $C_d$  value of the injector described in this paper, the team performed a statistical analysis to determine a suitable tolerance for the injector in use.

In Section 4.7 will be shown the effect of both the uncertainties on the engine performances, in order to evaluate the predominant one.

### 3.9 Cooling

The aim of this study is to determine whether the engine can be successfully cooled using RP1 throughout its operational lifespan. The primary constraint of the cooling strategy is to prevent RP1 from overheating and exceeding its boiling point temperature limit<sup>[47]</sup>.

The approach chosen by the team involves conducting a global thermal analysis under initial conditions to ensure engine sustainability at  $t_0$ , taking into account changes in the  $O/F$  ratio until successful outcomes are achieved in the cooling process.

Afterwards, the cooling system designed for  $t_0$  was used at each time iteration step to check if the engine could be cooled during its operative life.

The authors adopted the Dittus-Boelter model to evaluate the heat transfer inside the engine. The model was utilized despite the Prandtl number values and the  $L/D$  ratio being slightly outside its validity range<sup>[36]</sup>.

#### 3.9.1 Modelling of Cooling Process

Due to the high temperature of the flow in the combustion chamber, the adopted cooling strategy consists in combining regenerative cooling using RP1 with a Thermal Barrier Coating until the throat, while for the diverging part radiative cooling is exploited. The solution of a TBC was chosen over film cooling because of the already existing decrease in fuel mass flow rate over time, as any additional loss in flow rate would further degrade the performances.

The model also considers the engine as discretized in three different side sections: the combustion chamber and the converging part up to the throat which are cooled by regenerative cooling, and the diverging part which is cooled by radiative cooling. In the first two sections the team evaluated the heat flux that the fuel had to dissipate and its subsequent temperature increment, checking at the end of the cooling jacket the final temperature of RP1 and verifying if it was below its limit temperature<sup>[47]</sup>:

$$T_{end_{cooling}} < T_{limit_{RP1}} = 650K \quad (16)$$

The heat dissipation for the regenerative cooling at the first two sections has been modeled using a nodal approach with the electrical analogy shown in Figure 4, considering five consecutive heat exchanging layers<sup>[48]</sup>:

- Convection in the gas side from the adiabatic wall temperature ( $T_{aw}$ ) to the TBC (also for the diverging part of the nozzle)
- Conduction through the TBC
- Conduction through the Bond Coat
- Conduction through the material wall
- Convection in the liquid side

For the radiative cooling in the divergent section of the nozzle, the team retrieved the wall temperature (note that the TBC and the bond are consistently present along the entire engine contour to prevent geometric discontinuities, even in the divergent section): this temperature served as the basis to compute the radiative heat flux and determining if it was enough to dissipate the heat flux generated by the gas within the engine.

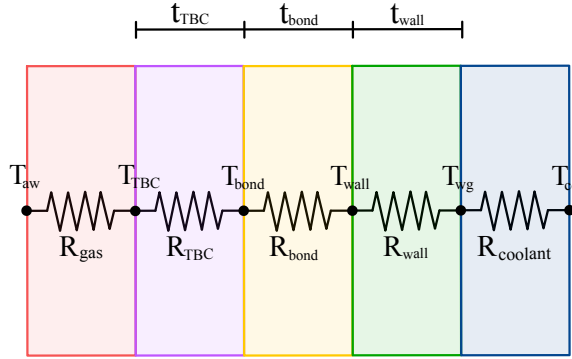


Figure 4: Equivalent electric circuit of the heat transfer model

## 4 Results

### 4.1 Nominal Engine Sizing

The nominal sizing was performed running firstly the NASA CEA Matlab function, and it gave the results reported in Table 2:

$M_c [-]$	$c_T [-]$	$P_e [Pa]$	$M_e [-]$	$v_e [m/s]$	$I_{spvac} [s]$
0.066	1.8786	1300	5.8473	3316.8	345.7

Table 2: Nominal NASA CEA results

It is possible to observe that the combustion chamber Mach number is almost zero, which is a good result in order to have an acceptable behaviour in the combustion chamber.

After computing the preliminary parameters, the geometrical sizing was computed (results reported in Table 3, Table 4, Table 5):

$A_t [m^2]$	$D_t [m]$	$A_c [m^2]$	$D_c [m]$	$A_e [m^2]$	$D_e [m]$
$1.0646 \cdot 10^{-4}$	0.0116	$9.5818 \cdot 10^{-4}$	0.0349	0.017	0.1473

Table 3: Areas and diameters

$\theta_{in} [deg]$	$\theta_{out} [deg]$	$r_{curv} [m]$
38	9	0.0022

Table 4: Rao angles and radius of curvature

$L_c [m]$	$L_{conv} [m]$	$L_{div} [m]$	$L_{tot} [m]$
0.12	0.0116	0.1772	0.3088

Table 5: Engine lengths

The volume of the cylindrical combustion chamber is  $V_c = 1.1498 \cdot 10^{-4} m^3$ .

Considering the project constraints, inside the cylinder there are the combustion chamber and the convergent part, for a total length inside the cylinder of  $0.1316 m$ .

From the initial parameters, it is possible to compute the mass flow rates at the starting stage:

$\dot{m}$ [kg/s]	$\dot{m}_{ox}$ [kg/s]	$\dot{m}_{fuel}$ [kg/s]
0.2948	0.2049	0.0899

Table 6: Mass flow rates

The mass flow rates are not high due to the low initial thrust and the exit velocity. These are trustworthy results, as the engine is a small liquid rocket engine and the areas of the injectors, later discussed in Section 4.6, have reasonable data.

From the nominal engine sizing, a CFD of the engine was performed, obtaining visual results of total temperature, total pressure and total energy.

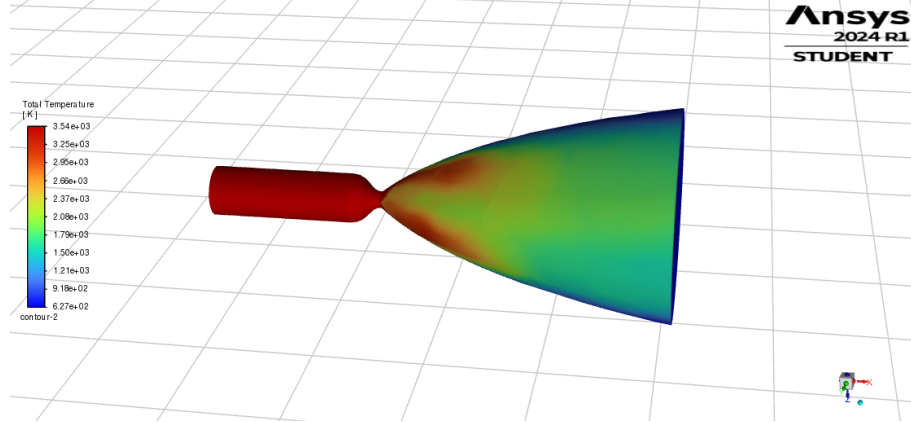


Figure 5: Total temperature CFD Simulation

The CFD workflow, the total pressure and total energy figures are visible in Appendix E.

## 4.2 Nozzle Efficiency

The engine sizing has been performed starting by an ideal nominal thrust of  $T = 1 \text{ kN}$ , without accounting for the losses in the nozzle that diminish the overall engine performance. This kind of approach was a team's choice, since calculating the losses in the divergent section of the nozzle required the definition of the geometries first.

The losses that the authors accounted for are:

- Divergent losses
- Boundary layer losses

The first one are due to the shape of the divergent section and the non axial-component of the exit flow (as stated in Section 2.3), the resulting equation is shown (Equation (17)):

$$\lambda = \frac{1 + (\cos(\frac{\alpha+\theta_e}{2}))}{2} \quad (17)$$

The second one, instead, concerns to the losses in the boundary layer of the flow passing through the nozzle; the discharge factor related to it has been computed analytically in Equation (18) by Tang [32]:

$$C_D = 1 - \left( \frac{\gamma + 1}{2} \right)^{\frac{3}{4}} \left[ 3.266 - \frac{2.128}{\gamma + 1} \right] Re'^{-\frac{1}{2}} + 0.9428 \frac{(\gamma - 1)(\gamma + 2)}{(\gamma + 1)^{\frac{1}{2}}} Re'^{-1} \quad (18)$$

where  $Re' = \sqrt{\frac{r_t}{r_c}} Re_t$  is the *modified throat Reynolds number*.

While the divergence losses remain constant with the geometry, the boundary layer losses change with the velocity in the throat; their nominal initial values and the resulting initial thrust are reported in Table 7:

$\lambda [-]$	$C_D [-]$	$T [N]$
0.9891	0.9999	989.32

Table 7: Initial values of correction factors and thrust

### 4.3 Tanks Sizing

The sizing of the tank has started thinking about the best configuration for their positions. The main driver for the selection was the symmetry of the configuration. In fact, even if not required, the team tried to have the most dynamically stable configuration possible and, to avoid too particular configurations, it has then been opted for a vertical stacking of two co-axial cylinders. This choice was related also taking in consideration the possibility to fill 80% of the available volume and the cylindrical shape is the best fit for a cylindrical space (see Appendix C).

The chosen configuration has taken the team to look for the maximum radius possible considering, though, that there should be an empty space for the pipelines to connect the upper tank to the combustion chamber. For this reason the lower tank will have a different radius with respect to the other.

The next step in the design of the tanks was the choice of the collocation of the liquid in the two tanks. The authors have opted for the configuration where the LOX is the liquid positioned the most far away possible from the combustion chamber. This decision was taken for multiple reason, but the main one is the fact that LOX is a liquid stored at very low temperature (90.14K) and, even if we are considering adiabatic tanks, keeping this fluid far away from the hottest part of the propulsion system is resulted being the best idea.

The material chosen to build the tanks is  $Ti - 6Al - 4V$  (TC4), a typical aerospace material that has optimum behaviours in cryogenic condition. This choice is related to the minimization of the mass of the tanks. Other metals were, in fact, thicker and heavier options, as shown in Table 11:

Temperature [K]	Yield Strength [MPa]	Ultimate Tensile Strength [MPa]	Density [kg/m <sup>3</sup> ]
298.14	761.2	847.9	4500
90.14	1099.0	1291.0	4500

Table 8:  $Ti - 6Al - 4V$  parameters at 90.14 K and 298.14 K<sup>[41]</sup>  
(90.14K values linearly interpolated)

The main problem of Titanium is that it might be reactive with LOX. The main reaction occur at higher temperature but this material is still one of the most dangerous to use with LOX<sup>[49]</sup>. Its reactivity at low temperature and high pressure is limited but the Titanium is still able to oxidize. Luckily, “*The presence of a stainless steel coating of any finite thickness which is physically intact would appear to preclude the possibility of LOX-titanium reaction*”<sup>[50]</sup>. So in this design it will be assumed an infinitesimal liner of Stainless-steel<sup>[51]</sup> that separates the Titanium alloy from the LOX in the tank, but it will not be considered in the calculations.

The same ratio is used for the volume of the gas in the two tanks (Equation (6)). The selection of the same ratio is taken trying to size the volume such as the pressure of the two different tanks remains the most similar possible for the whole period of time. This is achieved using the adiabatic formulas of the gas that expands in the tank.

Considering the specific case of a bipropellant system employing liquid Oxygen, Nitrogen’s solubility in LOX is a source of performance losses, thus Helium can be considered the best choice due to its inert characteristic and its low solubility in LOX<sup>[3]</sup>. In addition to this, with the adiabatic expansion

(Equation (5)), the temperature in the tank will fall and Helium has a lower boiling point than Nitrogen that would endanger the model.

Chemical formula	$\bar{R} [J/kgK]$	$\gamma [-]$
$He$	2077.3	1.667

Table 9: Helium parameters

The results of the sizing of the tanks, from the system of equation with Equation (7) is represented in Table 10:

Tank	$r_{int} [m]$	$th_{wall} [m]$	$h_{int} [m]$	$V [m^3]$	$M_{tank} [kg]$	$P [bar]$
<b>LOX</b>	0.4963	0.0037	0.8514	0.6589	70.1476	61.27
<b>RP1</b>	0.4749	0.0051	0.7940	0.5626	87.2197	60.99

Table 10: Sizing of cylindrical tanks

Tank	Al 2014 [kg]	304L Steel [kg]	Ti-6Al-4V [kg]
<b>LOX</b>	76.1519	88.0331	70.1476
<b>RP1</b>	175.1394	90.4676	87.2197

Table 11: Comparison of the masses with different materials

#### 4.3.1 Elliptic Headed Tanks

The computation of the elliptical headed tanks has taken more specific results shown in Table 12, in particular referring to the thickness of the surfaces in Table 13.

The aim was to have the maximum volume occupied, mainly to have a higher propellant mass. With this consideration it has been chosen the maximum height available for the tanks.

$$h_{available} = h_{tot} - L_c - L_{conv} - h_{empty-space} \quad (19)$$

where *empty space* is the needed vertical separation between combustion chamber-tank and tank-tank. Using the Volume ratio and the formulas of the elliptical heads<sup>[1]</sup>, the next step has been calculating the total volume inside the tanks.

The thickness study for this type of tanks is more precise, because, being a feasible option, the thickness of the wall changes depending on the position: in the *crown* (top part of the head) the thickness will be less than in the *knuckles* (welding point between head and cylindrical part). In addition to this, other factors are considered in this sizing, for example the weld efficiency ( $e_w$ ) of the material (for titanium alloys 0.85-0.95)<sup>[1][52]</sup>, and the knuckles stress factor ( $K$ ), that depends on the ellipse ratio ( $k = a/b$ ), taken from Figure 21 in Appendix D.

$$th_{crown} = \frac{P_{tank}ka}{2\sigma^y e_w} \quad th_{knuckles} = \frac{P_{tank}Ka}{\sigma^y e_w} \quad th_{cylinder} = \frac{(th_{crown} + th_{knuckles})}{K + k/2} \quad (20)$$

Tank	Radius [m]	Height [m]	Volume [ $m^3$ ]	Mass [kg]	Pressure [bar]
<b>LOX</b>	0.4900	0.9372	0.4605	100.1811	61.27
<b>RP1</b>	0.4700	0.8311	0.3501	117.691	60.99

Table 12: Sizing of headed tanks

Tank	$th_{crown}$ [m]	$th_{knuckles}$ [m]	$th_{cylinder}$ [m]
<b>LOX</b>	0.0061	0.0073	0.0061
<b>RPI</b>	0.0081	0.0101	0.0084

Table 13: Thickness in different surfaces of headed tanks

These tanks are still approximated, since it is not considered any thermal isolation or liners, but the values represented in Table 12 and Table 13 are reasonable, confirmed by literature and vendors catalogues<sup>[53]</sup>.

With these dimensions, the elliptical headed tanks volume, added to the volume occupied by the combustion chamber and the convergent nozzle, ends up occupying the 70.1277% of the total volume. This number is lower than the 80% available and confirms the choice taken of opting for cylindrical tanks.

#### 4.4 Nominal Configuration Results

The blowdown system main feature is the blowdown ratio. From the optimization in Section 3.6, a blowdown ratio of  $B = 3.1$  is obtained to guarantee the maximum burning time.

The team opted for this result, since it is in the blowdown range, that stands between 3 and 6.

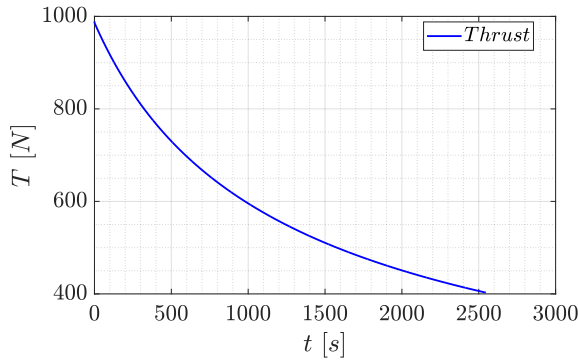


Figure 6: Thrust evolution

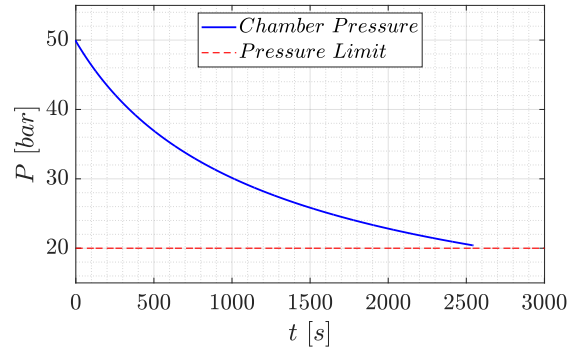


Figure 7: Chamber pressure evolution

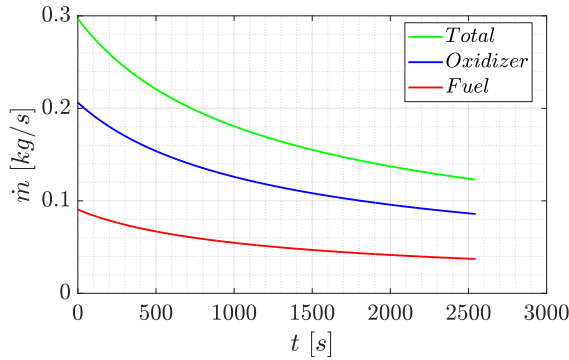


Figure 8: Mass flow rates evolution

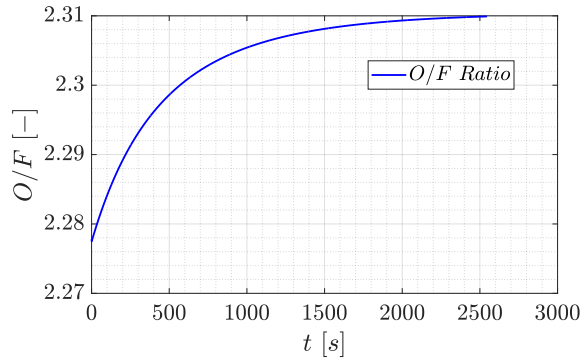


Figure 9: O/F evolution

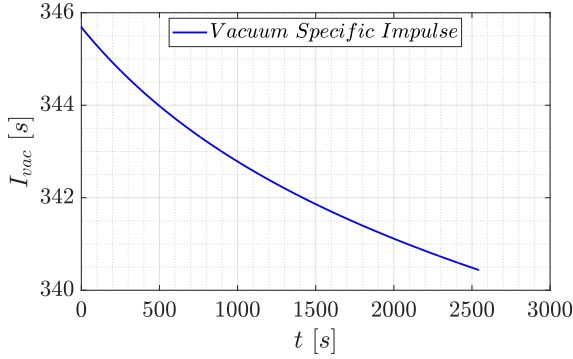


Figure 10: Vacuum specific impulse evolution

The blowdown pressurizing system changes in time the thrust, the specific impulse, the combustion chamber pressure, the mass flow rate and, consequently, the oxidizer to fuel ratio.

The thrust behaviour (Figure 6), considering the total burning time, decreases following the theory. This is due to the thrust thermodynamic formula that relates the total mass flow rate, the thrust coefficient and the characteristic velocity (Equation (15)). The main contribution, clearly, comes from the total mass flow rate, while the thrust coefficient and the characteristic velocity, which the code computes at each time step using the NASA CEA Matlab function, can be considered constants, as their variations in the total burning time are in the order of the last digits.

At this point, it is possible to compute the Total Impulse as the integral of the thrust in time:

$$I_{tot} = \int_0^{t_{burn}} T dt = 1673164.3 [Ns] \quad (21)$$

As we see in Figure 7, the combustion chamber pressure decreases too as the engine runs. This behaviour is supported by the thermodynamic relation that comprises the characteristic velocity, the total mass flow rate and the throat area (Equation (9)). As well as the thrust, the main contribution is done by the total mass flow rate, since the throat area is constant, while the characteristic velocity, as said in the thrust behaviour analysis, is practically constant.

Considering now the oxidizer and fuel mass flow rates, the trend decreases as the time goes from  $t = 0$  s to the burning time. The relation shows a dependency on the difference between the tank's pressure and the combustion chamber pressure, which lowers in time, and a dependency on the pressure losses coefficients (Equation (13)). The differences of pressures evaluating the two cases are almost the same, because the initial tanks' pressure are similar, while the coefficients vary due to the physical characteristics of the propellant components, having different densities and different injectors areas. Under these circumstances, it's clear the mass flow rates have different descendent rates. The oxidizer mass flow rate decreases faster than the fuel mass flow rate.

The oxidizer to fuel ratio is a direct consequence of the mass flow rates of the propellant components. Both the two mass flow rates decrease, and the oxidizer mass flow rate lowers faster, but the ratios increase due to the relation between the mass flow rates:  $\frac{O}{F} = \frac{\dot{m}_{ox}}{\dot{m}_{fuel}}$ .

Eventually, the specific impulse depends on the thrust and on the propellant mass flow rate. Both decrease, but it is possible to understand the specific impulse evolution due to the different descending ratios between the two parameters. The thrust, which is at the numerator, decreases faster than the mass flow rate, as seen in, so the behaviour is clarified.

## 4.5 Mass Budget

The mass budget is a critical parameter in the planning and execution of space missions, as it directly impacts the performance, cost, and feasibility of the mission. Moreover, the study of component masses has been instrumental in guiding our selection of materials for the construction of various engine components. The outcomes are displayed in Table 14.

Chamber & Nozzle [kg]	LOX Tank [kg]	RP1 Tank [kg]
0.7900	70.1476	87.2197
LOX [kg]	RP1 [kg]	He [kg]
370.1660	160.8151	13.7587

Table 14: Masses of the propulsion system

The total mass results in  $M_{tot} = 702.8971\text{ kg}$  and the dry mass in  $M_{dry} = 158.1573\text{ kg}$ .

## 4.6 Injectors Results

In accordance with the technical approach, the following results have been obtained:

Parameters	no. of Injectors [-]	$A_{inj} [\text{mm}^2]$	Injector Diameter [mm]	Injection velocity [m/s]
<b>LOX</b>	3	2.2004	1.70	27.225
<b>RP1</b>	6	0.6772	0.93	38.1693

Table 15: Injectors parameters

A preliminary evaluation has been conducted in order to determine the number of the triplets to manufacture in the injection plate. Indeed a higher number of elements leads to a more uniform mass distribution reducing the risk of combustion instability<sup>[13]</sup>. Nevertheless manifold designs increase the complexity of manufacturing and the probability to corrode the chamber's walls<sup>[54]</sup>. Therefore the team opted for a configuration involving three triplets.

Given the total area of the oxidizer and fuel injectors, along with their respective quantities, the areas and consequently the diameters of the individual oxidizer and fuel orifices were calculated. Both injector diameters adhere to the limitations imposed by additive manufacturing, namely a minimum diameter of 0.5 mm.

The fuel injectors create an impinging angle of 60 degrees, which avoids a high propellant back-flow and provides a good mixing<sup>[13]</sup>. The geometry selected for the single injector was the sharp-edged orifice, which yields a discharge coefficient  $C_d = 0.65$  considering that the orifice diameters are below 2.5 mm for both fuel and oxidizer<sup>[36]</sup>.

The velocities, computed using the continuity equation, fall within the values (10m/s – 50m/s) for which adequate mixing is ensured within the combustion chamber<sup>[36]</sup>. The impinging distance  $L_{imp}$  has been sized inverting the ratio  $L_{imp}/D_{ox}$ , which has been set to 5. The impinging distance obtained is  $L_{imp} = 4.64\text{ mm}$ . The ratio satisfies the requirement  $L_{imp}/D_{ox} \geq 5$ , ensuring the mitigation of excessive injector face heating, an issue that arises when  $L_{imp}/D_{ox}$  is too small<sup>[13][36]</sup>.

The injection head was made with the selective laser melting (SLM), an additive manufacturing technique. The material selected was the Inconel 718, a Nickel-Chromium-based superalloy, which has high melting point, useful for the face temperature of the injection head and the high heat flux. A material with high melting point is important, because it can avoid corrosion that can cause changes in orifices geometry or structural problems<sup>[13]</sup>. The choice fell also on this material because it is used in other space applications, like the injection head of Ariane 6 rocket<sup>[11][55]</sup>.

## 4.7 Analysis of Geometric Tolerances and $C_d$ Variations

In the following plots, the authors emphasize the impact of both geometric tolerances on the injectors' orifice diameters and the effect of tolerances on  $C_d$  resulting from the increased surface roughness associated with Additive Manufacturing.

The geometric tolerances, selected as  $\pm 50\text{ }\mu\text{m}$ , were assessed based on the data sheet as described in Section 3.8. Similarly, the absolute tolerances for  $C_d$ , determined as  $\pm 0.068$  through the statistical analysis outlined in Section 3.8, were also established.

In the plots, it is evident that the most unfavorable off-design condition occurs when considering the variation in  $C_d$ . This situation can be explained by considering the physical meaning of  $C_d$ .  $C_d$  accounts for the fluid dynamic losses within the injector conduits, thus it strictly depends on the surface finishing of the conduits obtained through additive manufacturing. Without considering the use of post-processing techniques to improve the obtained surface roughness, the surface finish will be of low quality. This results in increased turbulence within the conduits, leading to poorer mixing between oxidizer and fuel and consequently worse engine performance. Obviously, a better value of  $C_d$  lead to better performances for the exact opposite motivations.

The primary impact of geometric tolerances is observed in the values of the  $O/F$  ratio. Modifying the cross-sectional area of the injector orifices leads to changes in the mass flow rates of both oxidizer and fuel. This effect is particularly significant during the initial stages of engine operation, as the mass flow rate is higher at these times. However, during the latter stages of engine operation, the variation in  $C_d$  once again becomes the most significant factor.

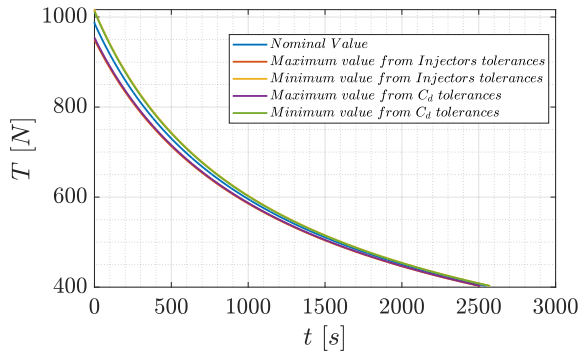


Figure 11: Thrust evolution

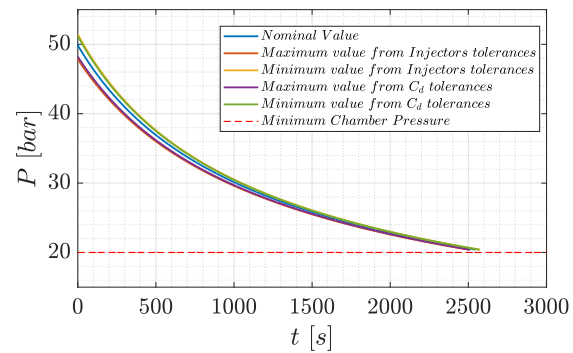


Figure 12: Chamber pressure evolution

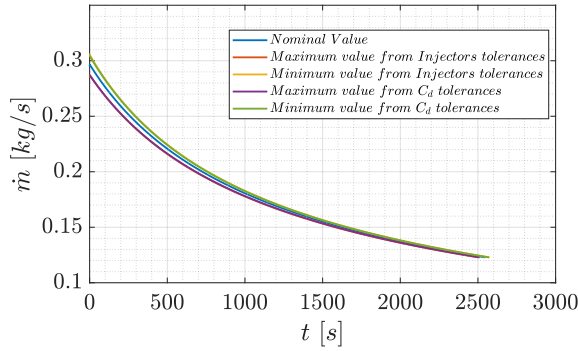
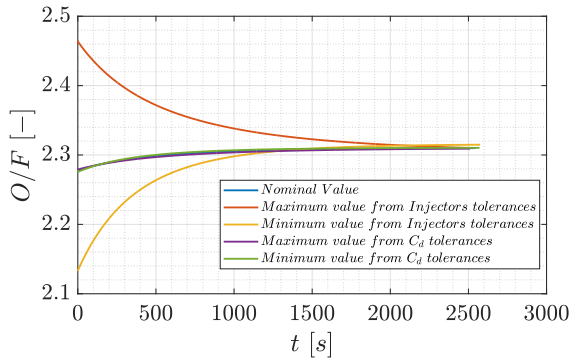


Figure 13: Mass flow rates evolution

Figure 14:  $O/F$  evolution

## 4.8 Cooling Results

As previously mentioned in Section 3.9, the heat dissipation for the regenerative cooling has been modeled considering five consecutive heat exchanging layers. The global heat transfer coefficient in the different sections is computed in Equation (22):

$$H_{global,A,B} = \frac{1}{\frac{1}{h_{g,A,B}} + \frac{t_{TBC}}{\lambda_{TBC}} + \frac{t_{bond}}{\lambda_{bond}} + \frac{t_{wall}}{\lambda_{wall}} + \frac{1}{h_{co,A,B}}} \quad (22)$$

where the convective heat transfer coefficients are computed in Equation (23) and Equation (24):

$$h_{g,A,B,C} = \frac{Nu_{A,B,C} \lambda_{gas,A,B,C}}{D_{A,B,C}} \quad (23)$$

$$h_{coA,B} = \frac{q_{A,B}}{T_{w_{co}} - T_{fuel_{A,B}}} \quad (24)$$

Having the convective heat transfer coefficient in the gas side, via Equation (25) it is possible to compute the heat flux exchanged by the gas inside the engine to the layer of TBC that needs to be dissipated:

$$q_{A,B,C} = \frac{h_{g_{A,B,C}}}{T_{aw_{A,B,C}} - T_{TBC}} \quad (25)$$

The team decided to opt for a TBC using  $Y_2O_3$ <sup>[56]</sup>, a Bond Coat of NiCrCuAl<sup>[57]</sup> glued to the Inconel X-750 walls<sup>[48][58]</sup>. The thermal conductivities are retrieved by the materials data shown in Section 4.8:

$\lambda_{TBC}$ [W/mK]	$\lambda_{bond}$ [W/mK]	$\lambda_{wall}$ [W/mK]
2	17	12

Table 16: Materials Thermal Conductivity

## 4.9 Sizing of the Regenerative Cooling System

The sizing process of the Regenerative Cooling System consists of computing the thickness of the different conductive layers and the diameter of the circular tubes in which RP1 flows to cool the engine.

**Layers Thickness** To compute the thickness of the layers, Equation (26) has been used:

$$q_A = \frac{\lambda_{layer}}{t_{layer}} \Delta T_{layer} \quad (26)$$

where  $\Delta T_{layer}$  for the different layers has been fixed taking the limit temperatures of the used materials as shown in Table 17 and  $q_A$  has been chosen as the team decided to keep constant thicknesses along the whole engine. The adiabatic wall temperature has been computed as shown in Ref.<sup>[36]</sup>.

$T_{TBC}$ [K]	$T_{bond}$ [K]	$T_w$ [K]	$T_{w_{co}}$ [K]
2000	1300	973	650

Table 17: Material limit temperatures

**Tubes Design** Also for the tubes diameter the team opted for a constant size through the whole cooling jacket. From Equation (24) the desired convective heat transfer coefficient  $h_{co_{des}}$  is retrieved. Then, knowing the characteristics of RP1 showcased in Table 21 in Appendix B it is possible to solve Equation (27) to compute the actual coefficient  $h_{co}$  which only depends on the choice of the hydraulic diameter of the tubes  $D_{hydr}$ :

$$\begin{cases} Nu = 0.243 Pr_{RP1}^{0.4} Re_{RP1}^{0.8} \\ Nu = \frac{h_{co} D_{hydr}}{\lambda_{RP1}} \end{cases} \quad (27)$$

The team iterated this process starting from an initial guess of the diameter and decreasing  $D_{hydr}$  until the exit condition was successful:

$$h_{co} \geq h_{co_{des}} \quad (28)$$

Subsequently, imposing a thickness of each tube of 0.5mm it was possible to retrieve the total number of tubes of the cooling jacket.

The final results of the sizing process are showcased in Table 18 and Table 19:

$t_{TBC}$ [mm]	$t_{bond}$ [mm]	$t_{wall}$ [mm]
0.42	1.68	1.17

Table 18: Layers thickness

$t_{tube}$ [mm]	$D_{tube}$ [mm]	$N_{tubes}$ [-]
0.5	2.1	36

Table 19: Tubes size

The sizes obtained for the cooling jacket and the layers are all technically feasible.

#### 4.9.1 Initial Cooling Validation

To perform a successful regenerative cooling of the engine a simple iteration process has been implemented. The process consists of computing the total heat flux that the fuel needs to dissipate and the subsequent temperature increase at the end of each section:

$$A_{side}H_{global} = c_{p_{fuel}}\dot{m}_{fuel}(T_{fuel_{end}} - T_{fuel_{in}}) \quad (29)$$

At the end of the process the cooling compliancy relation showcased in equation (Equation (16)) is checked and the  $O/F$  ratio is updated until the mass flow rate of fuel is enough to guarantee a proper cooling of the engine. A better representation of the iterative process is shown in Appendix B.

To provide satisfying results for the regenerative cooling, the team decided to decrease the  $O/F$  ratio to 2. Even though the nominal value of  $O/F = 2.2778$  used for the initial analysis was enough to meet the compliancy relation Equation (16), the team decided to decrease the  $O/F$  ratio to 2.

This decision was made to ensure proper cooling for a longer period of time from engine ignition, countering the decrease in fuel mass flow rate (Appendix B) over time by starting from a higher initial value. The temperatures at the beginning and end of each section are show in Table 20:

$T_{inlet}$ [K]	$T_{end_{chamber}}$ [K]	$T_{end_{cooling}}$ [K]
298.15	531.98	589.90

Table 20: Temperatures of RP1 during Nominal Cooling

The obtained results for  $T_{end_{cooling}}$  prove to be adequate with the cooling compliancy relation (Equation (16)).

#### 4.9.2 Cooling Compliancy during operative life

After having found the  $O/F$  ratio that guarantees proper cooling at the initial instant, a new sizing of the motor has been computed.

To check if the fuel is able to cool the engine even during its operative life, starting from the available  $\dot{m}_{fuel}$  at each time step of the blowdown iterative process the temperature of RP1 is retrieved and the cooling compliancy relation is verified (as better shown in Appendix B).

The team was thus able to calculate for how long the regenerative cooling of the engine would be feasible, before the mass fuel flow rate decreases too much.

The time evolution of  $T_{end_{cooling}}$  is showcased in Figure 15.

As can be seen, the cooling process proves to be compliant for about 460 seconds, until the decline in fuel mass flow rate becomes dominant, leading to the RP1 temperature surpassing its boiling point due to the heat flux generated within the engine.

#### 4.9.3 Radiative Cooling

The team opted to utilize Rhenium<sup>[59][60]</sup> as the material for the divergent section of the nozzle and calculated the radiative heat flux using Equation (30):

$$q_{rad} = \varepsilon\sigma T_w^4 \quad (30)$$

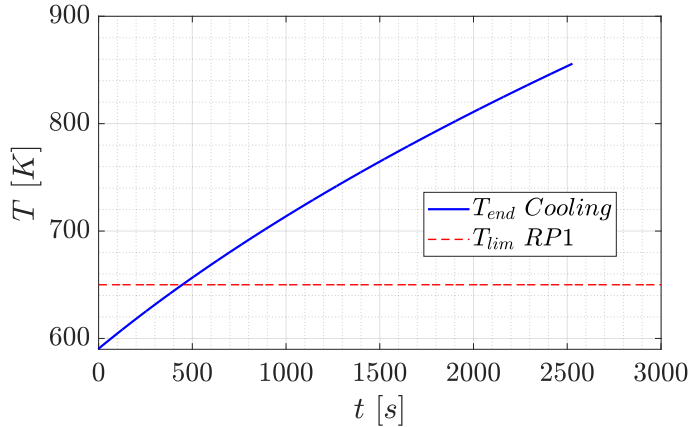


Figure 15:  $T_{end_{cooling}}$  time evolution

However, this heat flux proved insufficient to fully dissipate the heat generated from inside the nozzle.

While film cooling could have potentially solved this issue, its implementation was considered unfeasible due to the anticipated intensification of mass flow rate reduction, further compromising overall performance of the engine.

## 5 Final Considerations

The main objective of this study was to evaluate the performances of a bipropellant blowdown LRE. What the team expected, based on the theory studied in the course and the concepts found in the literature, was a decrease over time in Thrust and Pressure in the combustion chamber, attributed to the decrease in tank pressure due to the adiabatic expansion of the pressurizing gas.

The expected behaviour was confirmed by the implemented model, as showcased in Section 4.4.

For the chosen burning time, the team opted to determine it by selecting the blowdown ratio that maximized it. At this ratio, engine firing ceases upon reaching the minimum pressure of 20 bar (with a 2% margin). Lower blowdown ratios would have prematurely terminated engine operation due to constraints related to tank volume, a parameter more challenging to measure compared to chamber pressure, particularly under vacuum conditions.

Regarding the tanks, particularly the behaviour of the pressurizing gas, a more detailed analysis could have been to analyze the interaction of Helium with the two liquids.

The constraint of no post-machining refinement imposed to consider wider tolerances mainly in  $C_d$  leading to non-optimal off-design performances. Moreover, the analysis regarding the additive manufacturing production could have been extended to combustion chamber and nozzle.

For the injection plate, a rigorous mathematical analysis could have been performed to find the optimal number of triplets in order to maximize the uniform mass distribution without exceeding a fixed value of heat flux to the wall.

Analyzing the losses attributed to the boundary layer, the team anticipated a greater magnitude due to the miniaturization of the throat. Nonetheless, the high Reynolds number refuted this hypothesis.

For the cooling section, the authors implemented a system able of effectively cooling the engine for a satisfactory duration. However, due to overly strong approximations in the model and the omission of more conventional cooling techniques such as film cooling, the outcome proved to be non-optimal, suggesting potential future refinements in the analysis.

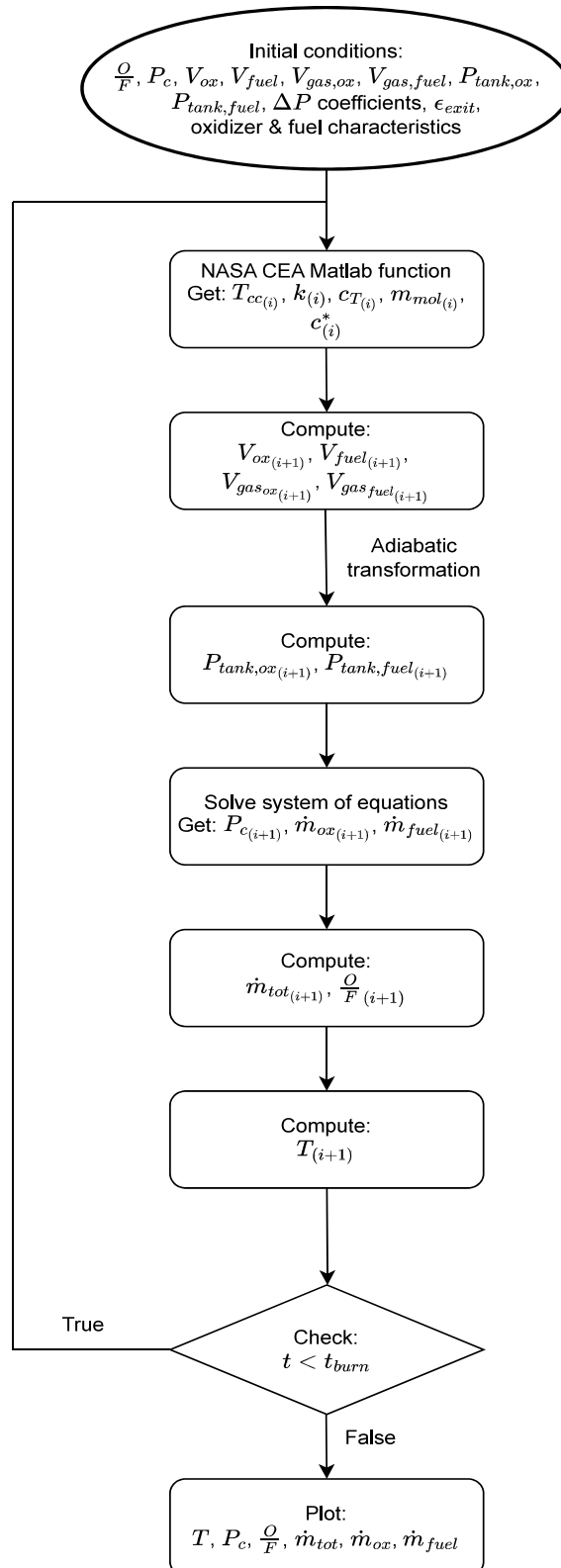
## 6 Conclusion

The precedent analysis presents the main features of the design of a blowdown bipropellant based engine, from the geometrical aspect of tanks, pipes, combustion chamber and nozzle to the evolution of the main physical parameters of the propulsion system. The blowdown model used to approach the problem allows to better understand the dependencies between the different quantities, expressed through the mathematical formulas, which result in the interactions between the single components of the system and its consequent global behaviour. Enhancing the knowledge about a blowdown bipropellant feed system, it was possible to exploit the importance of the optimal choice of the materials, with a special focus on the possibility and drawbacks of additive manufacturing processes. Several challenges to design the system were faced through different software simulating the engine response under different aspects, such as the cooling subsystem or the evolution of chemical reactions.

Afterwards, to proceed in the development of the LRE deeper analysis should be performed. The architecture of the system has to be fully defined: the ducts and the valves need to be selected and correctly designed to evaluate the precise pressure losses and the real shapes of the tanks should be refined to match the previously mentioned requirements. Furthermore, more accurate models simulating the chemical reactions should be taken into account to achieve better performances, since the presented frozen model do not consider the reactions occurring in the nozzle.

In the literature the option of the regulated pressure-fed system is actually preferred in past and current missions, therefore a comparison between the two architectures should be performed for the given thrust and chamber pressure. Otherwise, considering the computed burning time, to preserve the blowdown nature of the engine, a solution involving an extra gas tank for re-pressurization could be analyzed .

## A Blowdown cycle flux diagram



## B Cooling

**RP-1 Thermodynamical Properties**<sup>[47]</sup> [47]:

$\rho_{fuel} [kg/m^3]$	$\mu_{fuel} [Pa \cdot s]$	$\lambda_{fuel} [W/mK]$	$cp_{fuel} [J/kgK]$
799.67	$1.55010^{-3}$	0.11324	1880

Table 21: RP1 Thermodynamical Properties

### Fuel Mass Flow Rate reduction over time

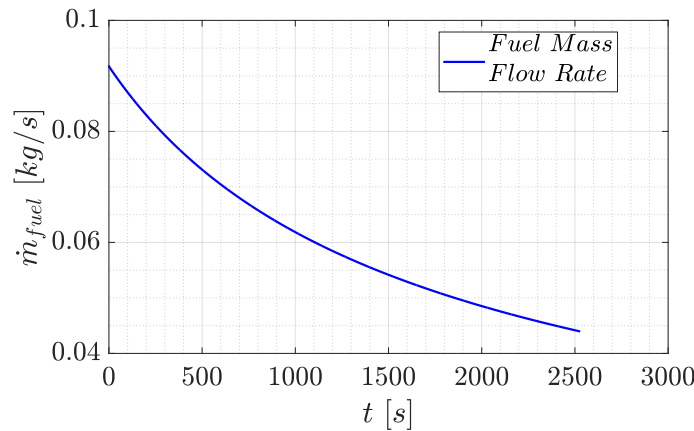


Figure 16:  $\dot{m}_{fuel}$  time evolution

### Tube sizing Algorithm

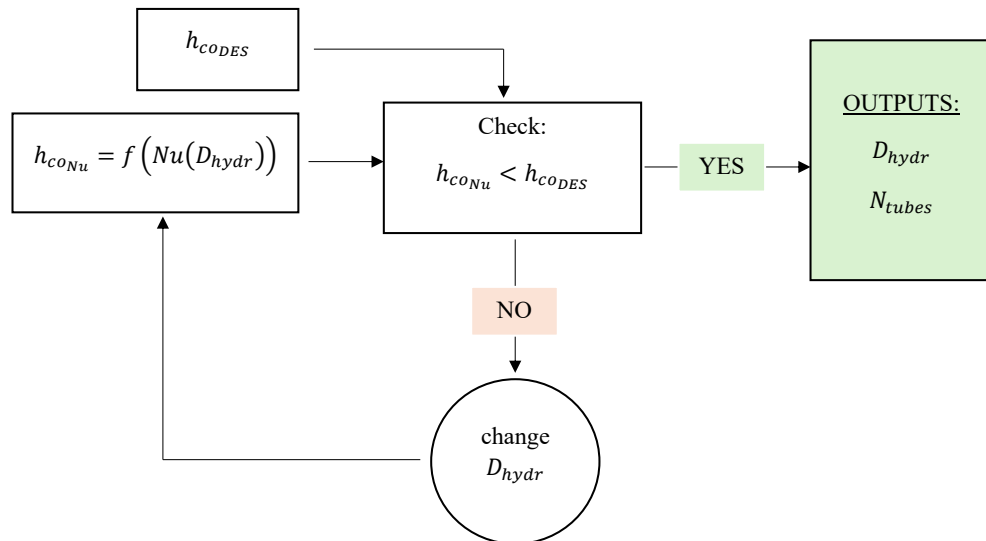


Figure 17: Sizing of the tubes hydraulic diameter flowchart

### Iterative Cooling Process Algorithm

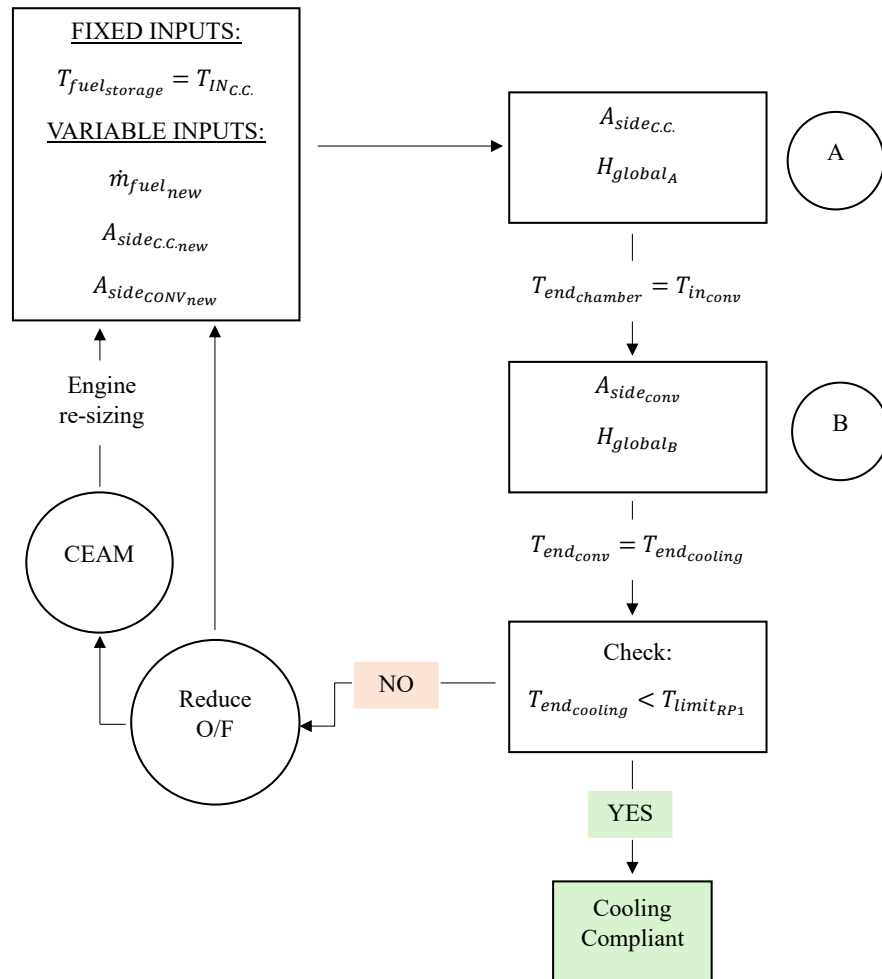


Figure 18: Cooling at  $t_0$  flowchart

## C Nominal design architecture

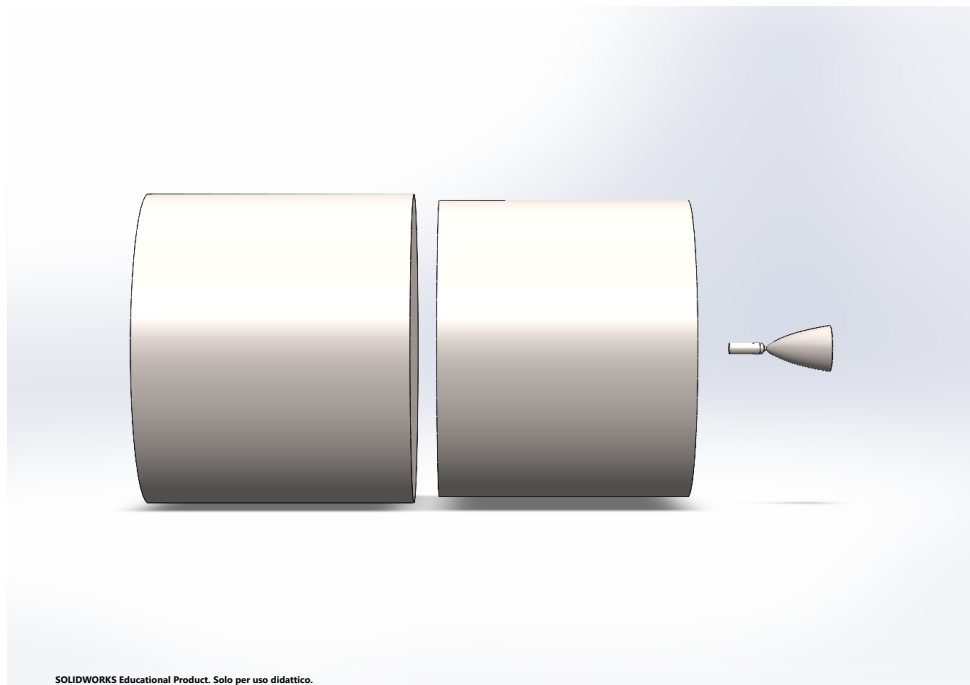


Figure 19: Nominal architecture: External view

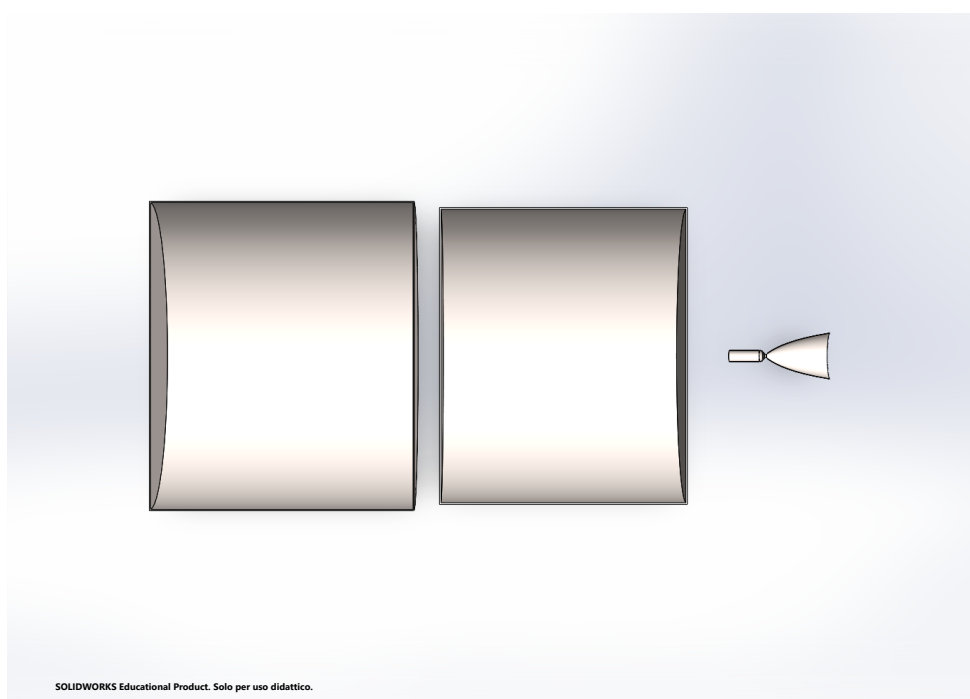


Figure 20: Nominal architecture: Internal view

## D Elliptic Headed Tanks Alternative

The computation of the geometrical and mechanical properties of the elliptic headed tanks has been evaluated basing the knowledge on NASA Design of Liquid Propellant Rocket Engines<sup>[1]</sup>. The geometrical design is divided in the cylindrical part and four ellipse heads. The height of the cylinder is chosen being the highest possible, as shown in Section 4.3, while the elliptic shape is taken with the highest possible ellipse ratio ( $k = a/b$ ) that corresponds to the most compact shape for the tanks.

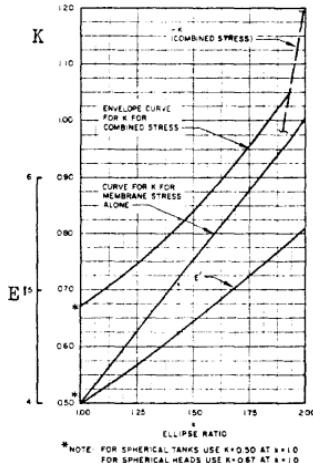


Figure 21: Knuckles stress factor (Table from page 338 Ref.<sup>[1]</sup>)

Here are represented the Oxidizer tank results and the CAD model :

Radius [m]	Height [m]	Volume [ $m^3$ ]	$th_{crown}$ [m]	$th_{knuckles}$ [m]	$th_{cylinder}$ [m]
0.4900	0.9372	0.4605	0.0061	0.0073	0.0061

Table 22: Sizing of elliptic headed oxidizer tank

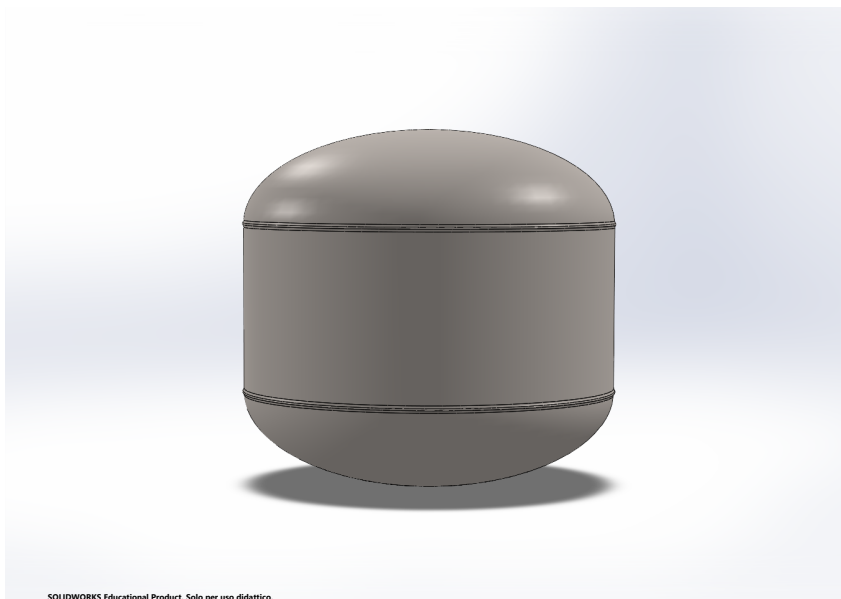


Figure 22: Elliptic headed tank: External view

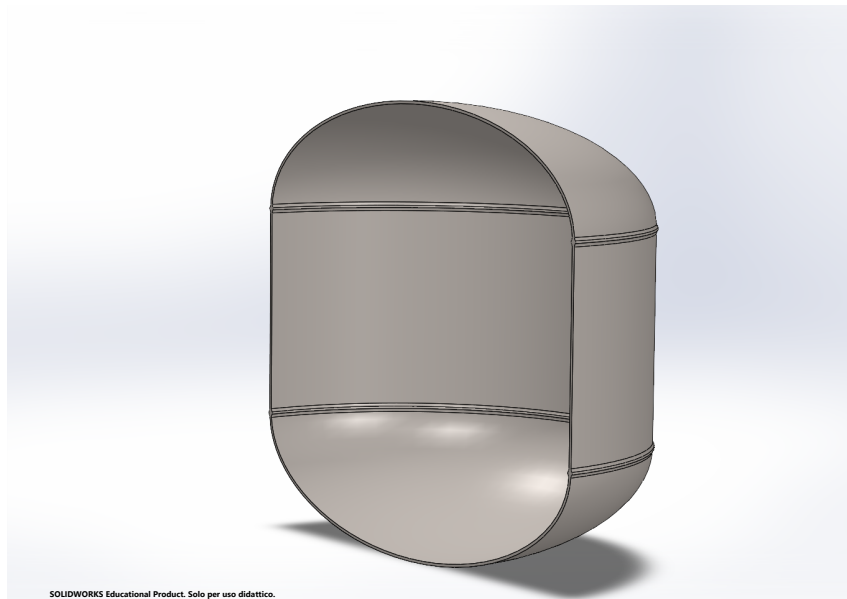


Figure 23: Elliptic headed tank: Internal view

## E Engine CFD simulation

The team computed the engine CFD using the Ansys Fluent application, in order to visualize the fluid flow, the heat and mass transfer, and the chemical reactions considering the nominal engine sizing.

The workflow starts with the problem identification, where the needed results, the options and the domain were defined. It was then created the solid model geometry using the SolidWorks application with the results obtained by the engine sizing. The mesh was generated importing the geometry on Ansys Fluent, deciding the number of cells, the cells geometry and various options with the aim of optimizing the solution with higher velocity and better accuracy.

The CFD options were then chosen, opting for:

1. Model energy: ON
2. Model viscosity: Inviscid
3. Model multiphase: OFF
4. Fluid: LOX – RP1

Adding the propellant main characteristics in Ansys Fluent

5. Boundary conditions:
  - (a) Inlet conditions: Pressure inlet
  - (b) Outlet conditions: Pressure outlet

The solution was computed with the default solution methods, choosing 200 iterations, an automatic time step method and a conservative length scale method.

The following images include the total pressure and the total energy. The total temperature can be found in Section 4.3.1 (Figure 5).

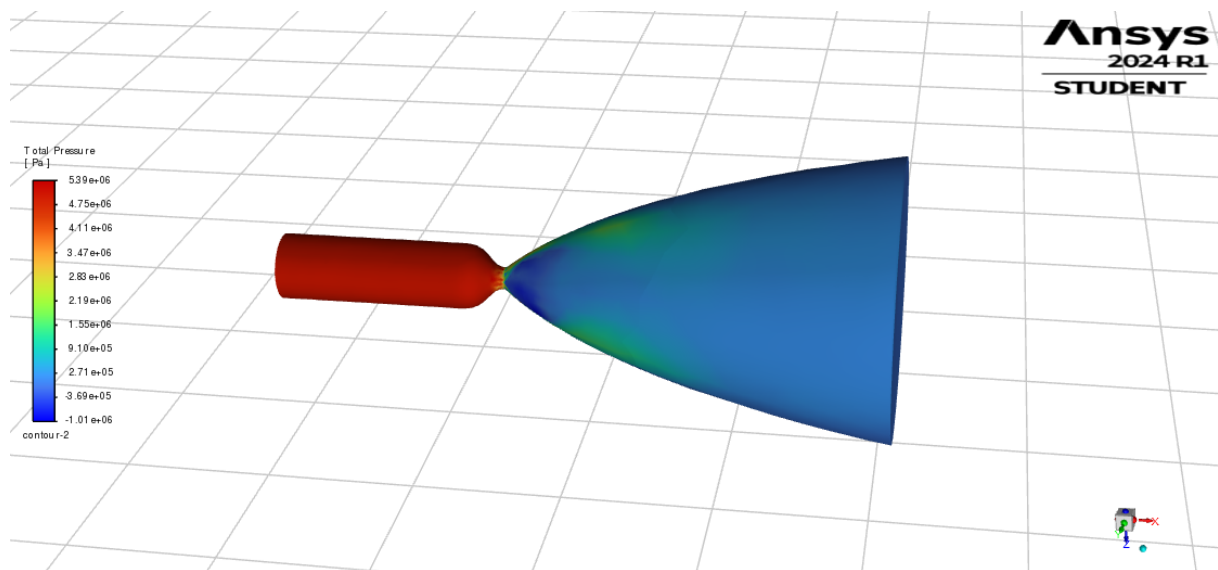


Figure 24: Total pressure CFD Simulation

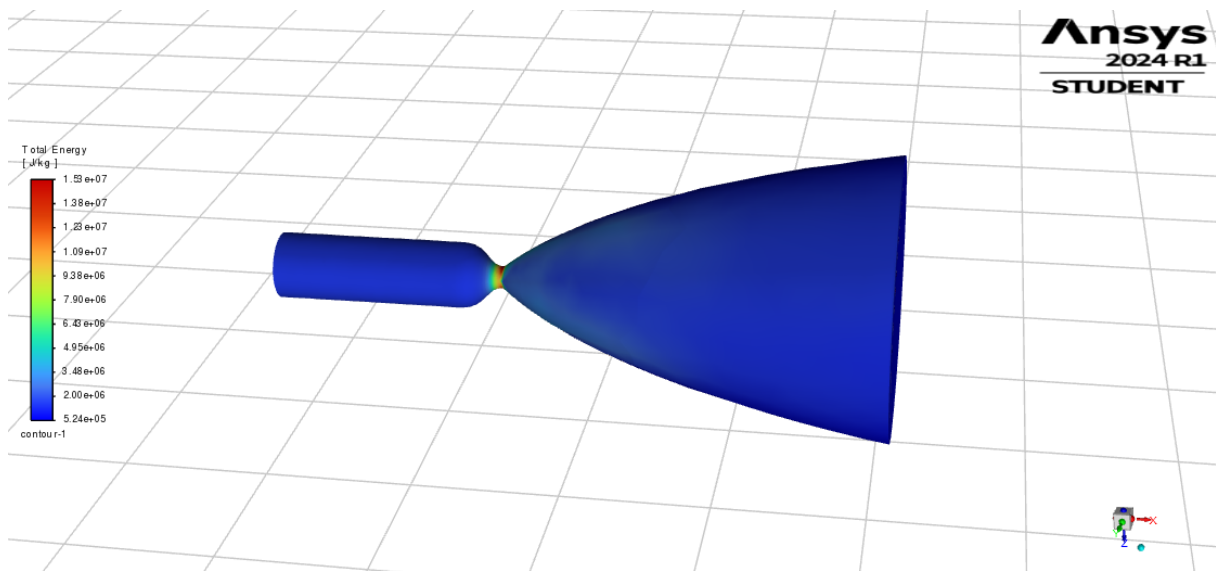


Figure 25: Total energy CFD Simulation

The results found with the CFD are in compliance with the outputs from the engine sizing. The temperature remains constant inside the combustion chamber, and drops in the divergent part from the higher value to a lower one, but not equal to the external temperature. The pressure has a similar behaviour, with a constant pressure inside the combustion chamber, a drop in the throat and an evolution until the lowest pressure. The total energy CFD shows the critical area in the engine, highlighting the thermal flux and energy variation in the throat.

## F References

- [1] H. Huzel, *Design of Liquid Propellant Rocket Engines, second edition.* NASA, 1967.
- [2] C. D. Brown, *Spacecraft Propulsion.* American Institute of Aeronautics and Astronautics, Inc, 1930.
- [3] G. Sutton and O. Biblarz, *Rocket Propulsion Elements, Ninth Edition.* John Wiley & Sons (US), 2017.
- [4] H. C. Hearn, “Feasibility of simple bipropellant blowdown systems,” *Journal of Spacecraft and Rockets, Volume 17, Issue 2*, 1980.
- [5] H. C. Hearn, “Thermodynamic Considerations in Bipropellant Blowdown Systems,” *Journal of Propulsion and Power, Volume 2, Issue 1*, 1984.
- [6] G. F. Pasley, “Prediction of tank pressure history in a blowdown propellant feed system,” *Journal of Spacecraft and Rockets, Volume 9, Issue 6*, 1972.
- [7] P. G. et al., “Additive manufacturing of liquid rocket engine combustion devices: A summary of process developments and hot-fire testing results,” AIAA Propulsion and Energy Forum, July 9-11, 2018, Cincinnati, Ohio, 2018 Joint Propulsion Conference. [Online]. Available: <https://ntrs.nasa.gov/api/citations/20180006344/downloads/20180006344.pdf>
- [8] B. Blakey-Milner, P. Gradl, G. Snedden, M. Brooks, J. Pitot, E. Lopez, M. Leary, F. Berto, and A. du Plessis, “Metal additive manufacturing in aerospace: A review,” *Materials & Design*, vol. 209, p. 110008, 2021. [Online]. Available: <https://www.sciencedirect.com/science/article/pii/S0264127521005633>
- [9] T. D. Ngo, A. Kashani, G. Imbalzano, K. T. Nguyen, and D. Hui, “Additive manufacturing (3d printing): A review of materials, methods, applications and challenges,” *Composites Part B: Engineering*, vol. 143, pp. 172–196, 2018. [Online]. Available: <https://www.sciencedirect.com/science/article/pii/S1359836817342944>
- [10] “ISO/ASTM 52911-1:2019(E) Additive manufacturing - Design - Part 1: Laser-based powder bed fusion of metals,” International Organization for Standardization, 2019. [Online]. Available: <https://www.iso.org/standard/72951.html>
- [11] EOS GmbH, “Additive manufacturing in aerospace: Case study by arianegroup.” [Online]. Available: [https://www.eos.info/01\\_parts-and-applications/case\\_studies\\_applications\\_parts/\\_case\\_studies\\_pdf/en\\_cases/cs\\_m\\_aerospace\\_arianegroup\\_en.pdf](https://www.eos.info/01_parts-and-applications/case_studies_applications_parts/_case_studies_pdf/en_cases/cs_m_aerospace_arianegroup_en.pdf)
- [12] A. Boschetto, L. Bottini, L. Macera, and S. Vatanparast, “Additive manufacturing for lightweighting satellite platform,” *Appl. Sci.*, vol. 13, p. 2809, 2023. [Online]. Available: <https://doi.org/10.3390/app13052809>
- [13] G.S.Gill, W.H.Nurick, *Liquid Rocket Engine Injectors.* NASA, 1976.
- [14] Terracciano, S. Carapellese, G. Bianchi, D. Liuzzi, M. Rudnykh, D. Drigo, F. Del Brusco, “Additive layer manufacturing technology in avio injector head design,” *7th European Conference of Aeronautics and Space Science, EUCASS 2017*, 2017.
- [15] S. Soller, R. Behr, S. Beyer, F. Laithier, M. Lehmann, A. Preuss, R. Salapete, “Design and testing of liquid propellant injectors for additive manufacturing,” *7th European Conference of Aeronautics and Space Science, EUCASS 2017*, 2017.
- [16] Z. Hu and S. Mahadevan, “Uncertainty quantification in prediction of material properties during additive manufacturing,” *Scripta Materialia*, vol. 135, pp. 135–140, 2017. [Online]. Available: <https://www.sciencedirect.com/science/article/pii/S1359646216305097>
- [17] J. Ilčík, D. Koutny, and D. Paloušek, *Geometrical Accuracy of the Metal Parts Produced by Selective Laser Melting: Initial Tests.* Springer, 04 2014, pp. 573–582.
- [18] Keller, Petr and Mendřický, Radomír, “Parameters influencing the precision of slm production,” *MM Science Journal*, vol. 2015, pp. 705–710, 09 2015.

- [19] T. Lieneke, G. A. O. Adam, S. Leuders, F. Knoop, S. Josupeit, P. Delfs, N. Funkel, D. Zimmer, “Systematical determination of tolerances for additive manufacturing by measuring linear dimensions.” [Online]. Available: [https://www.researchgate.net/publication/316827402\\_Systematical\\_Determination\\_of\\_Tolerances\\_for\\_Additive\\_Manufacturing\\_by\\_Measuring\\_Linear\\_Dimensions](https://www.researchgate.net/publication/316827402_Systematical_Determination_of_Tolerances_for_Additive_Manufacturing_by_Measuring_Linear_Dimensions)
- [20] B. E. Carroll, T. A. Palmer, and A. M. Beese, “Anisotropic tensile behavior of ti–6al–4v components fabricated with directed energy deposition additive manufacturing,” *Acta Materialia*, vol. 87, pp. 309–320, 2015. [Online]. Available: <https://www.sciencedirect.com/science/article/pii/S135964541400980X>
- [21] S. Khare and U. Saha, “Rocket nozzles: 75 years of research and development,” *Sādhanā*, vol. 46, 06 2021.
- [22] F. Malina, *Characteristics of the Rocket Motor Unit Based on the Theory of Perfect Gases*. J. Franklin Inst., 1940.
- [23] J. Berton, “Divergence thrust loss calculations for convergent-divergent nozzles: Extensions to the classical case,” 1991.
- [24] C. E. Rogers, “Departures from ideal performance for conical nozzles and bell nozzles, straight-cut throats and rounded throats,” *High Power Rocketry Magazine*, October 2004.
- [25] C. K. Murch, J. E. Broadwel, A. H. Silver, and T. J. Marcisz, “Performance losses in low-reynolds-number nozzles,” *J. Spacecraft*, vol. 5, no. 9, 1968.
- [26] L. Schoenman and P. Bloc, “Laminar boundary-layer heat transfer in low-thrust,” *J. Spacecraft*, vol. 5, no. 9, 1968.
- [27] C. B. Cohen and E. Reshotko, “The compressible laminar boundary layer with heat transfer and arbitrary pressure gradient,” NACA, Tech. Rep. 1294, 1956.
- [28] L. H. Back, P. F. Massier, and R. F. Cuffel, “Some observations on reduction of turbulent boundary-layer heat transfer in nozzles,” *AIAA Journal*, vol. 4, no. 12, pp. 2226–2229, December 1966.
- [29] D. R. Bartz, “A simple equation for rapid estimation of rocket-nozzle convective heat-transfer coefficients,” *Jet Propulsion*, vol. 27, pp. 49–51, 1957.
- [30] W. H. Garden, “Local heat-transfer coefficients in a nozzle with high-speed laminar flow,” Arnold Engineering Development Center, Tech. Rep. AEDC-TDR-64-61, April 1964.
- [31] S. P. Tang and J. B. Fenn, “Experimental determination of the discharge coefficients for critical flow through an axisymmetric nozzle,” *AIAA Journal*, 1978.
- [32] S. Tang, “Discharge coefficients for critical flow nozzles and their dependence on reynolds numbers,” Ph.D. dissertation, Princeton University, 1969.
- [33] A. N. Sabirzyanova, A. I. Glazunova, A. N. Kirillova, and K. S. Titov, “Simulation of a rocket engine nozzle discharge coefficient,” *Izvestiya Vysshikh Uchebnykh Zavedenii*, 2018.
- [34] J. Boise Pearson, D. Brian Landrum, Clark W. Hawk, “Parametric study of solar thermal rocket nozzle performance,” Propulsion Research Center University of Alabama in Huntsville. [Online]. Available: <https://ntrs.nasa.gov/api/citations/19960016396/downloads/19960016396.pdf>
- [35] L3 Harris Fast.Forward., “Datasheet.” [Online]. Available: <https://www.rocket.com/sites/default/files/documents/Capabilities/PDFs/Bipropellant%20Data%20Sheets.pdf>
- [36] F. Maggi, *Lecture notes in Space Propulsion*, Politecnico di Milano - Aerospace Science & Technology Dept., 2024.
- [37] G. V. R. Rao, “Exhaust nozzle contour for optimum thrust,” *Jet Propulsion Archive*, 1958.
- [38] James J. Hansen, Mennatallah Hussein, Samuel Moehring, Maxwell Stauffer, Colton Acosta, John Daly, Nitish Chennoju and Patrick Imper, “Student design of a bipropellant liquid rocket engine and associated infrastructure,” Arizona State University, Tech. Rep., 2020. [Online]. Available: <https://doi.org/10.2514/6.2020-3918>

- [39] H. E. Boyer, T. L. Gall, Ed., *Metals Handbook, Desk edition*. American Society for Metals, 1984.
- [40] Y. Qiu, H. Yang, L. Tong, L. Wang, “Research progress of cryogenic materials for storage and transportation of liquid hydrogen,” *mdpi*, 2021.
- [41] Y. Khao, X. Li, W. Fang, “Microstructure and mechanical properties of tc4 titanium alloy at the temperature of 77k,” *mdpi*, 2023.
- [42] K. U. Demir, İ. Gökdag, A. Dağkolu, M. Sahin, “Shape and size optimization of an aerospace propellant tank,” 2023. [Online]. Available: [https://www.researchgate.net/publication/373901042\\_Shape\\_and\\_Size\\_Optimization\\_of\\_an\\_Aerospace\\_Propellant\\_Tank](https://www.researchgate.net/publication/373901042_Shape_and_Size_Optimization_of_an_Aerospace_Propellant_Tank)
- [43] A. M. Cismilianu, M. Nastase, I. C. Oncescu, “Research on the optimal shape of high-pressure tanks for vehicles with vertical take-off and landing,” 2021. [Online]. Available: [https://www.scientificbulletin.upb.ro/rev\\_docs\\_arhiva/full70f\\_646957.pdf](https://www.scientificbulletin.upb.ro/rev_docs_arhiva/full70f_646957.pdf)
- [44] Namkyung Cho, Ohsung Kwon, Youngmog Kim, Sangkwon Jeong, “Investigation of helium injection cooling to liquid oxygen under pressurized condition,” 2006.
- [45] 3D Systems, “Direct metal printing brochure,” [https://www.3dsystems.hu/content/pdf/dmp\\_brochure\\_09.20.16\\_usen\\_web.pdf](https://www.3dsystems.hu/content/pdf/dmp_brochure_09.20.16_usen_web.pdf), 2016.
- [46] I. Müller, M. Kuhn, I. Petkov, S. Bletsch, K. Huybrechts, and P. Van Cauwenbergh, “3d-printed coaxial fuel injector for a lox/kerosene rocket engine,” 05 2018. [Online]. Available: [https://www.small-launcher.eu/wp-content/uploads/M%C3%BCller-3d-printed-coaxial-injector-for-a-LOX-kerosene-rocket-engine-SP2018\\_176-Sevilla-2018.pdf](https://www.small-launcher.eu/wp-content/uploads/M%C3%BCller-3d-printed-coaxial-injector-for-a-LOX-kerosene-rocket-engine-SP2018_176-Sevilla-2018.pdf)
- [47] J. Magee, T. Bruno, D. Friend, M. Huber, A. Laesecke, E. Lemmon, M. McLinden, R. Perkins, J. Baranski, J. Widegren, “Thermophysical properties measurements and models for rocket propellant rp-1: Phase i,” 2007-02-01 00:02:00 2007.
- [48] H. Huzel, *Design of Liquid Propellant Rocket Engines, second edition*. NASA, 1967.
- [49] Defense metals Information center, “Reactivity of metals with liquid and gaseous oxygen,” *NASA*, 1963.
- [50] K. E. Meiners, “Mechanical properties and lox compatibility of stainless steel-clad titanium prepared by explosive welding and vacuum deposition,” *NASA*, p. 63, 1969.
- [51] C. Ferrero, C. Marinari, E. Martino and R. Monforte, “La caratterizzazione strutturale dei materiali a temperature criogeniche,” 1993.
- [52] A. F. Norman, N. Iqbal, A. Robelou, K. Nor, D. Andrews, J. Martin, S. Dodds, R. Bellarosa, M. Meisnar, T. Ghidini, “Advanced manufacturing of titanium propellant tanks for space applications part 1: tank design and demonstrator manufacturing,” *CEAS Space Journal*, 2021.
- [53] N. GRUMMAN, *Diaphragm Tanks Data Sheets – Sorted by Volume*. [Online]. Available: <https://www.northropgrumman.com/space/diaphragm-tanks-data-sheets-sorted-by-volume>
- [54] James J. Hansen and Mennatallah Hussein and Samuel Moehring and Maxwell Stauffer and Colton Acosta and John Daly and Nitish Chennuju and Patrick Imper, “Student design of a bipropellant liquid rocket engine and associated infrastructure.” [Online]. Available: <https://arc.aiaa.org/doi/abs/10.2514/6.2020-3918>
- [55] K. Sajun Prasad, Sushanta Kumar Panda, Sujoy Kumar Kar, Mainak Sen, S.V.S. Naryana Murty, and Sharad Chandra Sharma, “Microstructures, forming limit and failure analyses of inconel 718 sheets for fabrication of aerospace components,” *Journal of Materials Engineering and Performance*, vol. 26(4), pp. 1513–1530, 2017.
- [56] V. Vázquez, “Material and manufacturing selection for rocket combustor testing prototype,” Ph.D. dissertation, Aeronautical University in Queretaro, 11 2021.
- [57] M. Baeker and T. Fiedler, “Stress evolution in thermal barrier coatings for rocket engine applications,” *Mechanics of Advanced Materials and Processes*, vol. 1, 12 2015.

- [58] “Material data for ninc35,” <https://asm.matweb.com/search/SpecificMaterial.asp?bassnum=NINC35>, accessed on April 13, 2024.
- [59] B. Reed, J. Biaglow, and S. Schneider, “Advanced materials for radiation-cooled rockets,” *Pennsylvania State Univ., NASA Propulsion Engineering Research Center*, vol. 2, 1993. [Online]. Available: <https://ntrs.nasa.gov/citations/19940018579>
- [60] D. T. F. Marple, “Spectral emissivity of rhenium,” *Journal of the Optical Society of America*, vol. 46, no. 7, 1956.

## **G Authorship Declaration**

**Alessandro Massini:** Literature Review (nozzle losses), Cooling System Design

**Edoardo Mensi Weingrill:** Literature Review (additive manufacturing), Injector Plate Design, Off-design analysis

**Marco Cattaneo:** Injector Plate Design, Nominal Engine Sizing, Computational Codes

**Luca Frassinella:** Nominal Engine Sizing (*RPA*), Cooling System Design

**Davide Bellini:** Tank Sizing, Optimal Blowdown Ratio study, Blowdown iterative process

**Giacomo Biraghi:** Blowdown iterative process, CFD simulations

**Mattia De Marco:** Literature Review (blowdown architecture), Blowdown iterative process

**Gianluca Scudier:** Injector Plate Design, Literature Review (nozzle losses), CFD simulations

**Camilla Bergamaschi:** Tank Sizing, Nominal Engine Sizing